An assessment of commercial CFD turbulence models for near wake HAWT modelling

O'Brien, J. M., Young, T. M., Early, J. M., & Griffin, P. C. (2018). An assessment of commercial CFD turbulence models for near wake HAWT modelling. *Journal of Wind Engineering and Industrial Aerodynamics*, *176*, 32-53. https://doi.org/10.1016/j.jweia.2018.03.001

Published in:
Journal of Wind Engineering and Industrial Aerodynamics

Document Version:
Peer reviewed version

An assessment of commercial CFD turbulence models for near wake HAWT modelling

J.M. O'Brien[a], T.M. Young[a], J.M. Early[a], P.C. Griffin[a,*]

[a] *School of Engineering, University of Limerick, Castletroy, Limerick, V94 T9PX, Ireland*
[b] *School of Mechanical and Aerospace Engineering, Queens University, Belfast, BT7 1NN, Northern Ireland*

Abstract

The simulation of the complex flow in a wind turbine wake is a challenging problem. To date, much of the research has been inhibited by both the time and computational costs associated with turbulence modelling. Additionally, the majority of numerical investigations focus on turbine performance and therefore neglect the near wake of a Horizontal Axis Wind Turbine (HAWT) entirely. This investigation focuses on experimentally and numerically quantifying the near wake structure of a model HAWT. The Shear Stress Transport (SST) $k-\omega$, Elliptical-Blending Reynolds Stress Model (EB-RSM) and the Reynolds Stress Transport (RST) turbulence models were used to model a turbine wake in the current study, with the results verified against experimental hot-wire data. Near wake velocity and turbulence characteristics were investigated to determine if low-order models can accurately predict the magnitude and distribution of velocity and turbulence values in the near wake of a model HAWT. The HAWT model was operated at two TSR values of 2.54 and 3.87. All models predicted velocity deficit values to within 2–4% and 4–7% of experimental results for TSR values of 2.54 and 3.87 respectively. Results showed that all models were able to accurately predict the mean velocity deficit generated in the near wake. All models were able to predict the fluctuating u and v velocity components in the near wake to the correct order of magnitude with the fluctuating velocity components having an inverse Laplace distribution in the wake. However, all models under-estimated the magnitude of these velocity values with predictions as low as -43% of experimental results.

Keywords: Wind turbine aerodynamics, SST k-ω turbulence model, Reynolds Stress Transport turbulence model, Computational Fluid Dynamics, Hot-wire Anemometry

1. Introduction

Up until recently, most aerodynamic modelling of wind turbines has been greatly simplified, with only a few researchers [1, 2, 3, 4] simulating the full turbine structure. The application

*I am corresponding author
Email addresses: jerry.obrien@ul.ie (J.M. O'Brien), trevor.young@ul.ie (T.M. Young), j.early@qub.ac.uk (J.M. Early), philip.griffin@ul.ie (P.C. Griffin)

of Computational Fluid Dynamics (CFD) models have been hindered due to the complexity associated with modelling the relative motion between rotating and stationary turbine components [5]. In addition, high performance computational resources are often not available, which results in CFD models being highly simplified. These simplifications include neglecting the tower structure or just modelling one turbine blade, taking advantage of the 120° periodicity [6, 7, 8, 9]. Such models are not able to model the unsteady phenomena associated with rotor tower/nacelle interaction, which has been shown to contribute very high levels of turbulent kinetic energy and Reynolds stress in the wake [10, 11]. Removing the tower from numerical simulations has a direct impact on the wake structure and velocity deficit experienced behind a turbine. Not only does this corrupt the structure of the rotor wake, but the increased turbulence leads to a faster reduction of the velocity deficit in the lower half of the turbine wake. With respect to future wind turbine structural modelling attempts, an understanding of the spatial distribution of stresses generated within the wake is important. The fluctuating velocity components in the flow directly contribute to the unsteady forces acting on turbine blades [5].

Noted in a review by O'Brien et al. [5], due to limited resources, most models are solved using steady time [12, 13, 14, 15, 9, 7, 8]. The transient effects of tower interaction, dynamic stall and wake meandering are difficult to model when using steady simulations [16, 17]. A study by Gomez-Iradi et al. [1] simulated rotor/tower interference for an upwind configuration turbine. This work simulated the displacement of the upwind stagnation point and boundary layer separation points of the tower at a periodic frequency of three times per revolution (for a three-bladed rotor). This resulted in periodic lateral loading of the tower. This pulsating displacement of the stagnation point was not observed in steady simulations.

Primarily, near wake research (particularly numerical research) is focused on power production and turbine performance [18]. However, this can be attributed to the fact that most numerical models are validated against earlier experimental works, which, as noted by Vermeer et al. [18] focused on HAWT performance. Additionally, most numerical models are validated against the NREL Phase VI measurement campaign of Hand el al. [19], which only investigated aerodynamic rotor loads and pressure distributions over the blades [5]. The current investigation focuses on the study of the near wake with a particular emphasis on the near wake structure. The near wake is taken as the area just behind the rotor, where the properties of the rotor can be discriminated [18]. The current investigation aims to validate numerical models against detailed near wake measurements of a full model turbine structure.

Wake turbulence, especially in a wind farm setting, contributes to the unsteady loading on wind turbine blades. As noted by Zhang et al. [20], limited information about the spatial distribution of turbulence and vortex behaviour in the near wake hinders the capability of the engineering community to predict wind turbine power production and fatigue loads in wind farms. However, our understanding of such engineering quantities is further reduced if the limitations of current turbulence modelling strategies with regards to predicting these phenomena is not explored. However, keeping computational costs in mind, there are newly

released models available such as a new Elliptic Blending Reynolds Stress Model (EB-RSM) released by STAR CCM+ as noted by O'Brien et al. [5]. This model was developed to meet industrial needs whereby it is more detailed than two equation eddy-viscosity models, but not as costly as a Reynolds Stress Transport model. This is accomplished by use of the elliptic relaxation concept proposed by Durbin [21], whereby the redistributive terms in the Reynolds stress equations are modelled by an elliptic relaxation equation. This model could provide a compromise between cost and accuracy for future HAWT modelling attempts. Detailed investigations of the near wake are valuable, especially for the validation of numerical models as the near wake structure effectively provides the "building blocks" for far wake analysis. However, to date, such measurements in the near wake are very rare [18, 22]. Finally, for future research regarding full scale modelling of HAWTs, the aerofoil data associated with large scale blades is often not available due to commercial sensitivity. Therefore, it is necessary to assess direct modelling techniques to ensure they accurately predict wake characteristics, as opposed to ADM (Actuator Disk model) and ALM (Actuator Line model) techniques. ADM and ALM were both neglected in the current study as they both rely on the BEM method in order to compute body forces. BEM methods are highly reliant on the aerofoil data chosen and dependant on empirical corrections to 2D aerofoil data.

In order to accurately model turbulence in any flow simulation, accurate modelling of the boundary layer of a solid surface is important. Interaction between airflow and a solid surface is in many engineering applications the origin of turbulence. In most commercial CFD codes this is usually done by the allocation of pressure-strain relationships. However, many pressure-strain relationships are dependant on y^+ wall treatments, which influence not only the ability of the solver to resolve the boundary layer, but also how it applies wall functions within the boundary layer to mimic turbulence dissipation rates and the two-component turbulence limit. The review by O'Brien et al. [5] has noted that many numerical simulations of HAWT wakes have been carried out, with mesh refinements in most cases taking y^+ values into consideration. The pressure-strain relationship and wall treatment used in these studies is often not mentioned, which has a major impact on a turbulence model's ability to solve for turbulence in the flow. No study has yet been carried out (to the knowledge of the authors) to access the ability of different pressure-strain relationships to accurately model turbulence in HAWT wakes. This is essential for future FSI simulations, as noted by Zhang et al. [20]. Additionally, modelling of flow/solid-surface interaction is the most expensive and difficult part of any CFD simulation. Investigating different pressure-strain relationships and how they impact the accuracy of a turbulence model could be used to determine the least expensive approach to HAWT wake modelling.

This study aims to investigate the ability of low-order turbulence models to accurately predict the turbulent characteristics of HAWT wakes. The ability of low-order turbulence models to predict the turbulence characteristics of HAWT wakes, speaks to their suitability for use in future FSI simulations of HAWTs.

The objectives of this study are as follows:

- To carry out an experimental measurement campaign in a wind tunnel of the near wake of a model Horizontal Axis Wind Turbine (HAWT) structure in order to validate numerical codes.
- To model, using advanced transient CFD the wake of the model HAWT to capture the development of a HAWT near wake including the root vortex structure.
- To establish a meshing strategy for near wake analysis.
- To assess the ability of the SST k-ω model (coupled with the Vorticity Confinement model), the EB-RSM and the RST model to accurately represent the mean and fluctuating velocity characteristics of the near wake.

2. Experimental Setup

2.1. Wind Tunnel Facility

This investigation was carried out in a closed loop return wind tunnel at Queens University, Belfast. The wind tunnel (see figure 1) has an enclosed test section of 0.85 m (height) x 1.15 m (width) x 3 m (length) with optically transparent side walls and can operate to a maximum freestream velocity of 40 m/s. For the current investigation, the wind tunnel had an average background freestream turbulence intensity of 0.19%. The turbine model was mounted 0.75 m from the test section entrance.

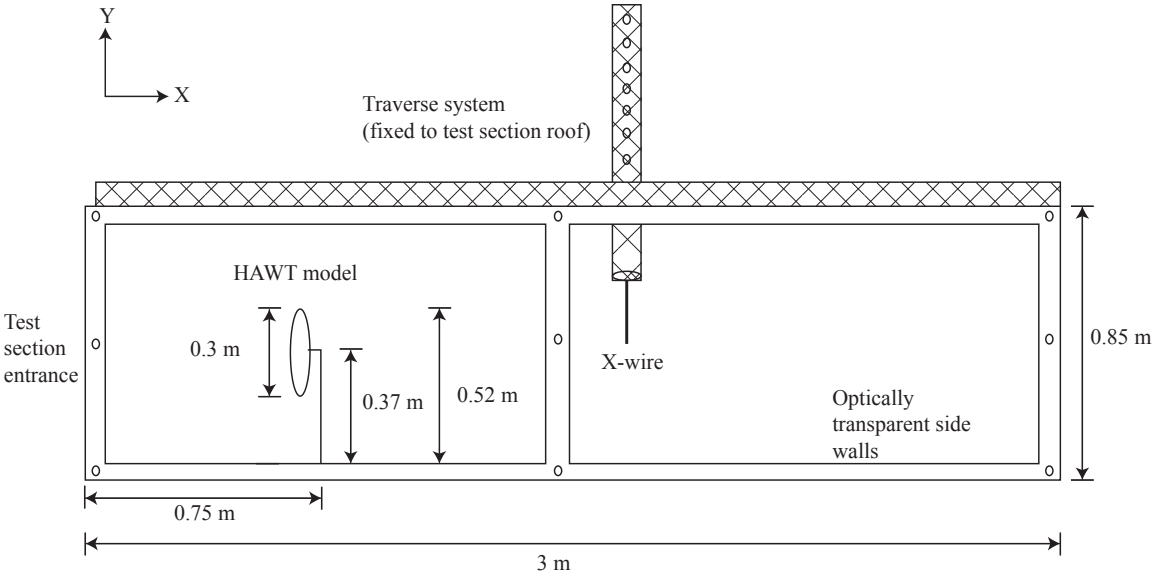

Figure 1: Wind tunnel schematic

2.2. Wind Turbine Model

The wind turbine model used for the present study was a three-bladed horizontal axis wind turbine. The turbine model was designed taking into account the Wind Atlas Analysis and Application Program (WAsP) wake model of [23], where the wind turbine wake is assumed to expand linearly with distance downstream. The wind turbine model has a rotor diameter of 0.3 m and a hub height of 0.37 m. Images of the turbine model and the main geometric parameters are given in figure 2. The blockage ratio for this study, defined as the ratio of the blade swept area to test section cross-sectional area is 7.22%. This was consistent with previous studies as the blockage ratio varies between 1-10% with 10% being the upper-most limit [24, 25, 26, 27, 28, 29]. The 10% upper limit criteria in this design was also based on a study carried out by McTavish et al. [30], which identified that the expansion of the near wake of a HAWT was not significantly modified if the blockage ratio remained between 6–10%. Values greater than 14% caused the wake to narrow by 35% [30].

The rotor blades for this study have a continuous FFA-W3-241 blade profile. The blades are twisted linearly with a pitch angle of 10° at the tip and 35° at the root. The chord of the blades also tapers linearly, with a tip chord of 10 mm and a root chord of 30 mm. The turbine model has a cone and tilt angle of 0° and the rotor plane was perpendicular to the free stream at all times. The turbine was rotated by a brush-less DC electric motor, which was controlled via a speed controller. During experimentation the turbine was run at two Tip Speed Ratios (TSR): 2.54 (1622 rpm) and 3.87 (2465 rpm). It should be noted that the turbine model freely rotated at a TSR of 2.54 with no input from the DC electric motor (optimum TSR). The rotational speed of the turbine was monitored using a high speed camera. A highly reflective tape was fixed to the rotor hub and was recorded using the high speed camera. All images were recorded at a frequency of 2 kHz which allowed for the rotational speed of the turbine model to be calculated and monitored during experiments.

The inlet velocity profile was recorded one diameter upstream of the turbine model before wake velocity measurements were taken. The wind speed was found to be 10 m/s at hub height (i.e. U_∞=10 m/s). This free stream velocity value was kept constant for all measurements. This resulted in a Reynolds number range of 21.7×10^3 to 20.4×10^3 and 20.8×10^3 to 29.9×10^3 for TSR of 2.54 and 3.87 respectively. The Reynolds number was based on the tip chord length of 10 mm. The Reynolds number and relative velocity definition are given in equations 1 and 2,

$$Re = \frac{c_{tip} V_{rel}}{\nu} \tag{1}$$

$$V_{rel} = U_\infty \sqrt{(1-a)^2 + \left(\frac{r\Omega_r}{U_\infty}(1+a')\right)^2} \tag{2}$$

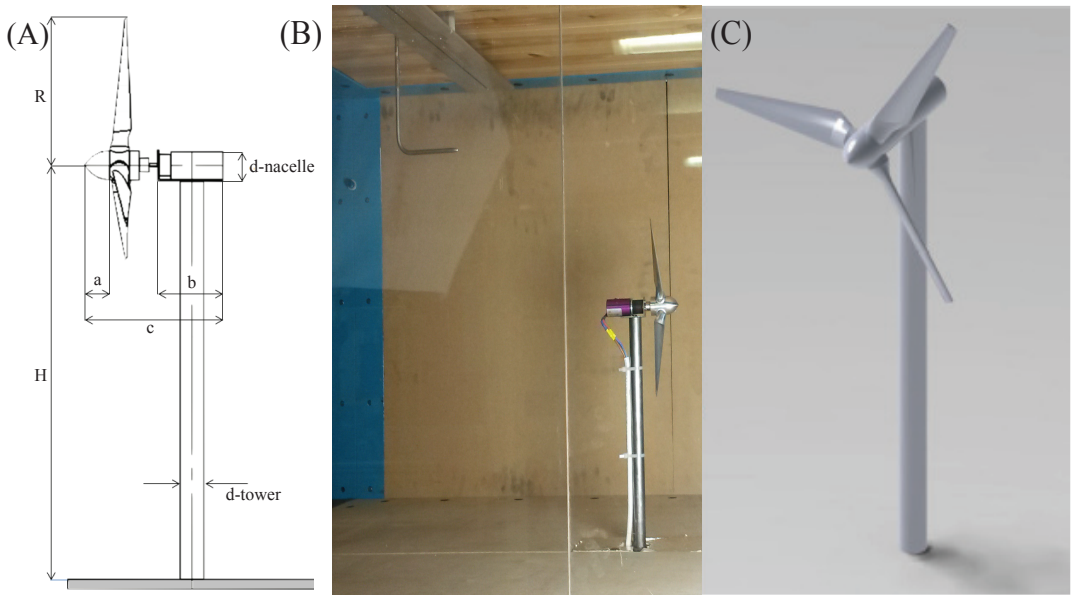

Parameter	R	H	a	b	c	d-nacelle	d-tower
Dimension (m)	0.15	0.37	0.025	0.072	0.15	0.026	0.024

Figure 2: Schematic (A), physical (B) and numerical (C) images of the wind turbine model used in the current experimental investigation

where a and a' are the axial and tangential interference factors, ν is the kinematic viscosity of air, r is radius and Ω_r is rotational velocity.

Few experiments regarding the near wake have been undertaken with most been performed at low Reynolds numbers (as related to blade chord and rotational speed). Despite these types of experiments not resembling a full-scale turbine, they can be used to verify numerical models [18]. The fundamental behaviour of the helical tip vortices and turbulent wake flow downstream of wind turbines is almost independent of the chord Reynolds number [31, 6, 11]. Performance characteristics were not recorded for the current study as the main focus was to investigate mean and fluctuating velocity components as opposed to performance.

2.3. Velocity Measurement Techniques and Experimental Uncertainty

All velocity measurements were recorded using a two-component hot-wire x-probe. The Constant Temperature Anemometry (CTA) system used in this study was a TSI IFA 300 system with a Dell Optiplex GX620 computer and THERMALPRO software. All measurements were recorded with a TSI 1240-T1.5 5 μm x-wire. In an attempt to capture the root vortex system, a measurement grid spacing of 1 cm across the entire rotor plane was adopted. This resulted in 30 measurement points across the rotor diameter and a total of 1558 data points per plane. The probe was mounted to a two-axis traverse system, which was attached to the roof of the test section. The mean percentage errors associated with

the x-probe were less than 3% for velocities between 0 m/s and 3 m/s and less than 1% for velocities greater than 3 m/s, as computed by the THERMALPRO software. The sampling rate and time for the hot-wire probe were 1 kHz and 1 s respectively. Velocity measurements were recorded in 3 separate planes ($0.66D$, $1D$ and $1.5D$) downstream from the rotor plane (where D is defined as the rotor diameter). A numerical representation of the measurement planes is shown in figure 3.

The recording time of 1 s at each recording location corresponded to measurements recorded for 27 and 41 full rotor revolutions. The transient flow disturbances are the vortex shedding from the tower and the rotational effects of the turbine. The vortex shedding from the tower was estimated to be in the region of 83 Hz based on a Strouhal number of 0.2 (circular cylinder) and the rotation of the turbine corresponded to 27-41 Hz, so in sampling at 1 kHz the likelihood of these effects dominating the signal is reduced. Given the large volume of data that was collected in this study a 1 s sampling duration per grid point location in the planes downstream of the turbine was considered adequate. This would eliminate any transience in the recorded data and proved a statistically averaged data for comparison to numerical data.

3. Numerical Simulation

3.1. Introduction

All simulations were carried out using the finite volume solver Star CCM+ and were solved using a HPC cluster (Fionn) of the Irish Centre for High-End Computing (ICHEC). Both the SST $k-\omega$ and RST models (EB-RSM model included) were run using 192 cores respectively. All models simulated $2s$ of physical time with a timestep value that represented one degree of rotation. The timestep used in this study is similar to that used by Li et al. [3] and Valiadis et al. [32]. Convergence criteria were enabled on the x, y and z-momentum equations, turbulent dissipation and kinetic energy equations (only applied to the SST $k-\omega$ model). These convergence criteria prevented the solution from advancing to the next timestep until the residual values reduced below 1×10^{-4}. Residuals in Star CCM+ are a measure of the imbalance of the conservation equations and the degree to which their discretized form is satisfied. In effect, they represent the solution error of a particular variable. However, in Star CCM+ the residual errors are auto-normalized by its maximum recorded value in the first five iterations. The normalized residuals represent the order of magnitude in which these values fall from their peak values.

The RST and EB-RSM models did not have any convergence criteria enabled on the x,y and z-momentum criterion as the models proved to be numerically very robust. The RST model was unable to meet the previously mentioned x,y,z criterion after 132,000 iterations and therefore the models could not advance to the next timestep. This pointed to the solvers requiring additional steps within each timestep in order to solve the physics to a satisfactory level. For both RST and EB-RSM simulations, the number of inner iterations (defined as the number of iterations computed by the solver for a single timestep) per timestep was

increased to 10 from the default value of 5. Residual values reduced below 1×10^{-6} for both SST $k-\omega$ simulations and below 1×10^{-5} for all RST and EB-RSM simulations. The SST $k-\omega$, EB-RSM and RST models required 50 hours, 119 hours and 144 hours to complete respectively. All models were run using a 2^{nd} order central spatial discretization scheme with a double precision.

For all simulations, velocity point data was recorded using presentation grids. A presentation grid samples data from regularly spaced intervals on a finite plane. These are illustrated in figure 3. Velocity data were recorded in the same locations for both the numerical solution and experimental investigation. All velocity measurements were recorded after the solution domain had experienced two flow throughs. One flow through is defined as the length of time required for a fluid particle to enter and exit the solution domain. At this point each simulation had built up to a statistically steady state.

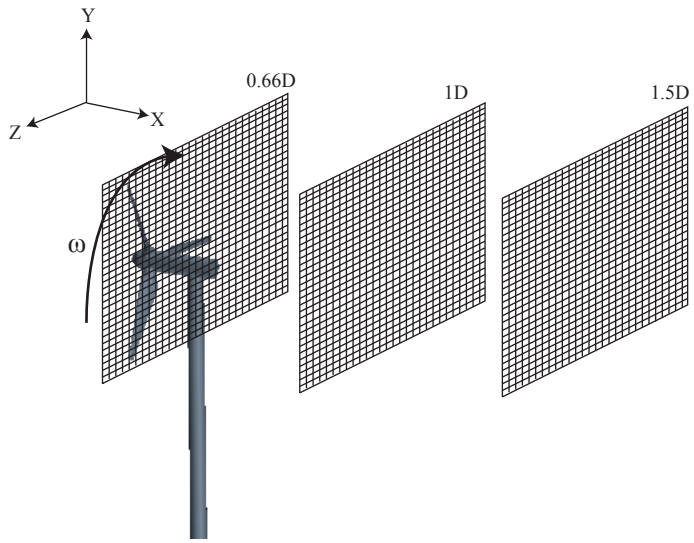

Figure 3: Positioning of presentation grids behind the wind turbine CFD model

3.2. SST k-ω Turbulence Model

Numerical simulations were firstly carried out using the implicit unsteady Shear Stress Transport (SST) $k-\omega$ turbulence model. SST is an aerospace industry standard turbulence model and is a good benchmark for higher fidelity models such as unsteady Reynolds Stress Transport (RST) and Large Eddy Simulation (LES) models. The governing equations for the SST k-ω model are the k and ω equations, given below as equations number 3 and 4, respectively, with the source terms omitted [33]. The reader is referred to Wilcox [33] for further information regarding the SST $k-\omega$ model.

$$\frac{\partial(\rho k)}{\partial t} + \nabla \bullet (\rho k \vec{U}) = \nabla \bullet \left[(\mu + \frac{\mu_t}{\rho_k}) \nabla k \right] + P_k - Y_k \tag{3}$$

$$\frac{\partial(\rho\omega)}{\partial t} + \nabla \bullet (\rho\omega\vec{U}) = \nabla \bullet \left[(\mu + \frac{\mu_t}{\rho_\omega})\nabla\omega\right] + P_\omega - Y_\omega + D_\omega \tag{4}$$

The shortcomings of eddy viscosity models representing highly complex rotational flows has been well documented [34, 35, 36]. However, attempts have been made to overcome the shortfalls of the $k-\omega$ model by adding correction terms. For the current study, the $k-\omega$ model was coupled with curvature correction terms using second order discretization and the Vorticity Confinement Model of Steinhoff [37] and later refined by Löhner [38]. The curvature correction term supplies the effects of strong curvature and frame-rotation by altering the turbulent energy production term according to local rotation and vorticity rates. This term is applied as vortices tend to dissipate early with two equation models. The Vorticity Confinement Model adds a forcing term (f_ω) to the momentum equations in all directions in order to preserve the vortex – see equations 5 and 6, which highlight the addition of f_ω to the momentum equation in the x-direction.

An example of the modified x-direction momentum equation is defined as

$$\frac{\partial u}{\partial t} + \nabla \bullet (u\vec{\mathbf{u}}) = -\frac{1}{\rho}\frac{\partial p}{\partial x} + \upsilon\nabla \bullet (\nabla u) + f_\omega \tag{5}$$

where the forcing term is defined as

$$f_\omega = -\epsilon\rho\,(\hat{n} \times \vec{\omega}) \tag{6}$$

where $\vec{\omega}$ is vorticity, ϵ is a user-defined constant (default value of 0.04 for three-dimensional cases) and $\hat{n}$ is the unit vector. The flow was modelled as an unsteady turbulent gas, assuming constant density with a segregated flow model. An unsteady transient model was selected as the aerodynamic phenomena associated with wind turbine aerodynamics cannot be completely modelled when using steady time simulations.

3.3. Reynolds Stress Transport Turbulence Model

The RST turbulence model was used to investigate the accuracy of a Reynolds Stress Transport model coupled with the linear pressure-strain two-layer term modelled using the linear approach of Gibson and Launder [39] to predict the characteristics of a turbine wake. By solving the Reynolds Stress Tensor, this model naturally accounts for effects such as anisotropy, which is associated with swirling motion, streamline curvature and rapid changes in strain rate. The model does not use Boussinesq's eddy viscosity hypothesis to compute the Reynolds stresses, but instead solves transport equations for each of the six Reynolds stresses and a model equation for the isotropic turbulent dissipation ϵ. This is the same equation used in the standard k-ϵ turbulence model. The Reynolds stress transport equation from Versteeg et al. [40] is given in equation 7 with the isotropic turbulent dissipation ϵ given by equation 8. In equation 8, S'_{ij} represents terms from the fluctuating strain rate

tensor.

$$\overbrace{\frac{\partial\left(\rho\overline{u_i'u_j'}\right)}{\partial t}}^{UnsteadyTerm}+\overbrace{\frac{\partial}{\partial x_k}\left(\rho u_k\overline{u_i'u_j'}\right)}^{C_{ij}\equiv Convection}=-\overbrace{\frac{\partial}{\partial x_k}\left[\rho\overline{u_i'u_j'u_k'}+\overline{p(\delta_{kj}u_i'+\delta_{ki}u_j')}\right]}^{D_{T,ij}\equiv TurbulentDiffusion}$$
$$+\overbrace{\frac{\partial}{\partial x_k}\left[\mu\frac{\partial}{x_k}\overline{(u_i'u_j')}\right]}^{D_{L,ij}\equiv MolecularDiffusion}-\overbrace{\rho\left(\overline{u_i'u_k'}\frac{\partial u_j}{\partial x_k}+\overline{u_j'u_k'}\frac{\partial u_i}{\partial x_k}\right)}^{P_{ij}\equiv StressProduction}+\overbrace{\overline{p\left(\frac{\partial u_i'}{\partial x_k}+\frac{\partial u_j'}{\partial x_i}\right)}}^{\Pi_{ij}\equiv PressureStrain-Interaction} \tag{7}$$
$$-\overbrace{2\rho\Omega_k\left(\overline{u_j'u_m'}e_{ikm}+\overline{u_i'u_m'}e_{jkm}\right)}^{\Omega_{ij}\equiv Rotation}-\overbrace{2\mu\overline{\frac{\partial u_i'}{\partial x_k}\frac{\partial u_j'}{\partial x_k}}}^{\epsilon_{ij}\equiv Dissipation}$$
$$\epsilon=2\frac{\mu}{\rho}\overline{S_{ij}'S_{ij}'} \tag{8}$$

The RST model used the same physics continua at the SST k-ω model.

3.4. Pressure-Strain Term used in Reynolds Stress Transport Model

The pressure strain relationship is highly important regarding the subject of turbulence modelling. The computational complexity and expense of Reynolds Stress Models (RSM) models is often driven by the difficulty of modelling the effects of solid walls on adjacent turbulent flows. These effects include pressure fluctuations due to eddies interacting with each other with other areas of the freestream which have a different mean velocity.

The Linear Pressure-Strain Two Layer Term was investigated as the relationship is defined as a two-layer formulation which is suitable for low-Reynolds number flows. Essentially, the model was favoured as it allowed the RST model to use an all y^+ wall treatment which would be more suitable for the mesh used in this investigation.

This model extends the linear model of Gibson et al. [39] so that it can be applicable to the near-wall sub-layer where viscous effects are dominant. The extension allows the usual log-law/local equilibrium matching to be discarded and enables boundary-layer problems to be tackled where the flow structure in the inner region departs from what is usually termed the "universal" wall law [41]. As noted by Launder et al. [41], there are many situations where the application of local equilibrium conditions to turbulent stresses and energy dissipation rates near the wall is not appropriate as this condition would be too complex to enforce. For example, a study carried out by Launder et al. [42] highlighted that at high rotation rates, turbulent mixing near the suction surface was annihilated. This feature cannot be modelled if the wall-law approach is enforced. Additionally, streamwise pressure gradients, body forces, strong secondary flows and separation can cause the flow to deviate from "universal" wall behaviour [41].

The linear pressure-strain model used in this case expresses the pressure-strain term as three components:

$$\Pi_{ij} = \Pi_{ij,1} + \Pi_{ij,2} + \Pi_{ij,3} \tag{9}$$

The so called "slow" pressure-strain or "return-to-isotropy" term $\Pi_{ij,1}$ represents a physical process within the flow where there is a reduction of the anisotropic properties of the turbulent eddies due to their mutual interactions. The "rapid" pressure-strain term is defined as $\Pi_{ij,2}$. This terms supposes that the rapid pressure partially counteracts the effect of production to increase the Reynolds-stress anisotropy [43]. The "wall reflection" term is defined as $\Pi_{ij,w}$. This term is responsible for the redistribution of normal stresses near the wall. It damps normal stresses perpendicular to the wall, while enhancing stresses that are parallel to the wall. The reader is referred to Gibson et al. [39] for further information.

3.5. Elliptical Blending Reynolds Stress Turbulence Model

A more robust and industry-friendly Reynolds Stress model was developed by Manceau et al. [44]. It will be referred to as the Elliptic Blending Reynolds Stress Model (EB-RSM). The model was developed to meet industrial needs and was noted by O'Brien et al. [5] as a possible substitute to a full RST model for HAWT analysis. While simple and robust, the model preserves the elliptic relaxation concept proposed by Durbin [21] whereby the redistributive terms in the Reynolds stress equations are modelled by an elliptic relaxation equation. This method avoids the need to use damping functions at the wall. However, the model proposed by Manceau et al. [44] uses only one scalar elliptic equation instead of six as proposed by Durbin [21]. Durbin's original model consisted of six elliptic differential equations with boundary conditions to reproduce the near-wall behaviour of the redistributive term. The EB-RSM model is a low-Reynolds number model that is based on an inhomogeneous near-wall formulation of the quasi-linear Quadratic Pressure strain term. A blending function is used to blend the viscous sub-layer and the log-layer formulation of the pressure-strain term. This approach requires the solution of an elliptic equation for the blending parameter α. The EB-RSM model used in this investigation is based on the EB-RSM model of Meanceau [44] and revised by Lardeau et al. [45]. The main objective of the Elliptic Blending approach is to account for the influence of wall blockage effects towards the wall-normal component of turbulence, which is required to produce the two-component limit of turbulence at the wall.

The EB-RSM is based on a blending of near-wall and quadratic pressure-strain models for the pressure strain and dissipation, defined as follows:

$$\phi^{\star}_{ij} - \epsilon_{ij} = (1-\alpha^3)(\phi^{w}_{ij} - \epsilon^{w}_{ij}) + \alpha^3(\phi^{h_{ij}} - \epsilon^{h}_{ij}) \tag{10}$$

where $\phi^{\star}_{ij}$ is the pressure-strain tensor and ϵ_{ij} is the dissipation-rate tensor. The term α is a blending parameter. The blending parameter α is the solution of the following elliptic equation:

$$\alpha = L^2 \nabla^2 \alpha = 1 \tag{11}$$

whereby the solution of this equation goes to zero at the wall and close to unity far from the wall. The length-scale L defines the thickness of the region of influence of the near wall. The EB-RSM model used the same physics continua at the SST k-ω model.

3.6. Mesh Generation and Boundary Conditions

Figure 4 illustrates the computational domain used in this study. The flow direction is from left to right. The rotational domain refers to the area inside the outlined disc around the rotor, as illustrated in the magnified image in figure 4. The rotating domain includes the rotating blades, spinner and hub connections. The solution domain, turbine tower and nacelle combine to make the stationary region. The turbine nacelle was simplified in order to reduce the complexity of the mesh behind the rotating region of the turbine. The nacelle was modelled as a solid cylinder with a diameter of 0.026 m. Additionally, the computational domain length was extended to 4 m for the CFD model. This was done to take into account the outlet pressure criteria set at the domain outlet. Near the domain outlet the flow can still be turbulent. This could cause an interaction to occur at the pressure outlet boundary, which could result in reversed flow occurring in cells near the exit. Reverse flow occurs when the pressure in the cell adjacent to the outlet boundary is lower than the pressure specified on the boundary itself and the adverse pressure gradient is sufficiently large to cause the flow at the outlet to reverse direction, ie. flow enters the domain from the outlet. This is commonly caused by the specification of a uniform outlet pressure when the flow near the boundary is highly non-uniform. In this case, the outlet boundary was too close to geometric features that cause flow non-uniformity. This error is specified in the simulation output window and is monitored by the user. To help mitigate this issue, the outlet boundary was positioned further from the obstruction to allow the flow to become more uniform prior to reaching the outlet boundary. In this case the outlet of the domain was extended from 3 m to 4 m, which resolved the issue. There was no data recorded in the current study to investigate if reversed flow errors would have resulted in decreased accuracy of the simulation. The inlet was modelled as a velocity inlet with a free stream velocity value of 10 m/s and the freestream turbulence present was defined in the simulation physics. An Atmospheric Boundary Layer (ABL) was not modelled as it was deemed necessary to assess each models ability to predict wake characteristics with a uniform inlet velocity first. The introduction of an ABL would have complicated the simulation and make it difficult to determine if inaccuracies in the models were resulting from mesh quality, turbulence models and selected physics (vorticity confinement and pressure-strain relationships) or the addition

of turbulence in the freestream due to the ABL. In addition to this, using an ABL would result in further refinement of the simulation mesh in front of the rotor to ensure the ABL profile was resolved before entering the rotor. This would have increased the computational expense of the simulation.

The computational domain (top, bottom and both sides of the numerical wind tunnel) and the numerical HAWT were modelled as wall boundaries with a no-slip condition. The rotation of the turbine was modelled using the sliding mesh approach. This method requires a rotational velocity to be prescribed as a boundary condition on the solid rotor. The rotating and stationary regions of the solution were also connected by internal interfaces. Interfaces allow simulation quantities (such as mass, momentum and energy etc.) to pass between stationary and rotational regions. The RST and EB-RSM models were initially run in steady state using moving reference frames. This provided the solver with an initial solution which was then used in the unsteady case. Running the steady model beforehand reduced the risk of divergence of the unsteady solution.

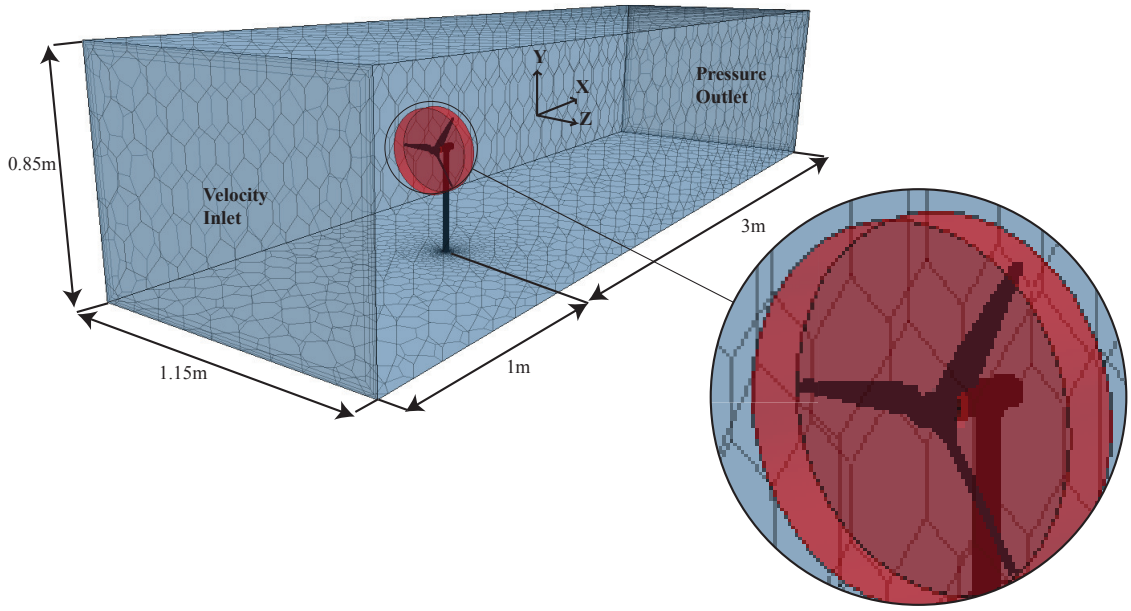

Figure 4: A schematic of the computational domain used in this study

For this simulation, an unstructured polyhedral mesh was used, as it is less computationally demanding than a tetrahedral mesh. Polyhedral cells are orthogonal to the flow regardless of flow direction. This makes them suitable for modelling highly rotational flows. Finally, due to the large number of sides (12 for a polyhedral cell), polyhedral meshes are suitable to mesh models that contain curved surfaces. Therefore, the polyhedral mesh was most suitable to model the highly curved and twisted surfaces of the turbine blades. For the purpose of this study, the mesh density for both the rotating and stationary regions were

treated separately. This can be accomplished by using the sliding mesh approach. This was accomplished by subtracting a cylinder within the solution domain (stationary region). The size of this cylinder is the same size as the rotor swept area. Within this area the rotor is imprinted within the simulation. Therefore, this allows the rotor and the stationary region to be meshed independently. This is advantageous as the turbine blades often need to be meshed to a higher density than the rest of the solution domain. The mesh density of the rotating region depended on a mesh sensitivity study, whereby an investigation was carried out into the variation of average surface pressure on the blades and y^+ values. The wake mesh was defined by investigating the maximum velocity deficit recorded behind the rotor at $0.66D$ for different wake mesh densities. The results of the mesh sensitivity study highlighting surface average pressure distribution over the rotor is presented in figure 5a. The red circles in figures 5a and 5b highlight the point where increasing cell density resulted in no change to the recorded engineering parameter observed. Following this study, the rotating region contained 4×10^6 cells using a base size of 38 mm. Beyond this count there was no appreciable change in the above-mentioned surface average pressure parameter. Curve controls were then used on the turbine blades to refine the mesh further towards the leading and trailing edge. This prevented the need for additional volumetric controls around the turbine blades and improved the resolution of vortex shedding and rollup. A final cell count of 4.28×10^6 was used for the rotating region.

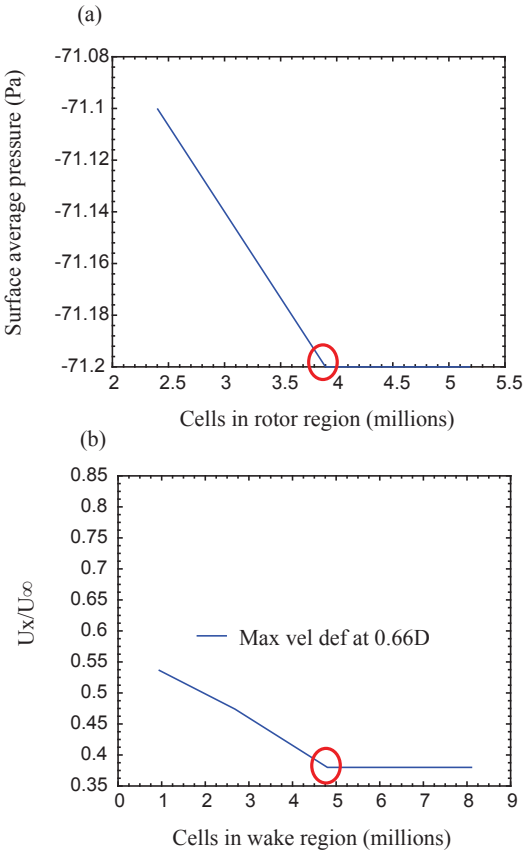

Figure 5: Mesh sensitivity results

The wake region was defined by a volumetric cone with a refined mesh density in order to capture the wake structure. The volumetric cone was sized, based on the WAsP wake model of Barthelmie et al. [23]. The maximum velocity deficit in the wake did not change after 4.75×10^6 cells. All mesh sensitivity simulations for the wake mesh were carried out with a rotor mesh density of 4.28×10^6 cells. However, the mesh density of the wake region was increased to 5×10^6 cells in order to have a volume change between the rotating and wake region of 1, as shown in figure 6. This reduced any inaccuracies caused by large changes in cell sizes between the regions. The simulation had a combined cell count of 9.29×10^6. A 2D section of the meshed solution domain can be seen in figure 7. It can be noted that the wake volumetric control extends 0.5D infront of the turbine model. This allowed for the flow to be resolved to a high degree of accuracy before entering the rotor plane. Additionally, by extending the volumetric cone ahead of the turbine rotor, this created a favourable volume change across the mesh in the regions of interest. A large jump in volume from one cell to another can cause potential inaccuracies and instability in the solvers. Extending the wake cone made it possible to create a conformal mesh across the interface between the rotating and stationary regions. A conformal mesh produces a high-quality discretization for the analysis and eases the passage of information between regions.

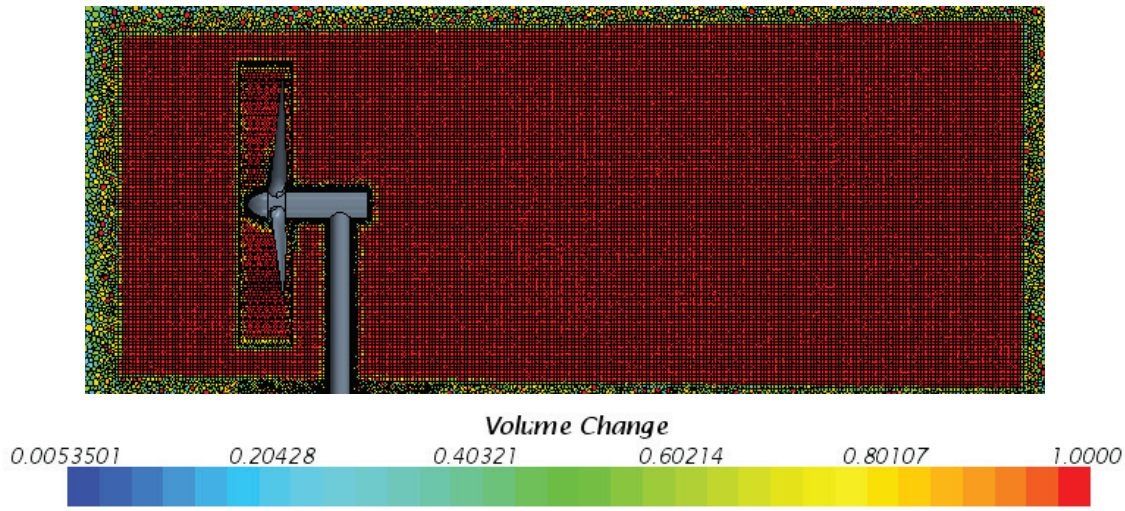

Figure 6: Volume change scalar scene

3.7. Wall Treatment

Within numerical simulations, walls are a source of vorticity and therefore, accurate prediction of flow and turbulence parameters across the wall boundary layer is essential.Star CCM+ uses a set of near-wall modelling assumptions known as "wall treatments", for each turbulence model. Different y^+ wall treatments are used within Star CCM+ for different mesh resolutions near a wall boundary. Wall treatments are used to mimic the dimensionalless velocity distribution inside the turbulent boundary layer.

Wall treatments in Star CCM+ are divided into 3 categories. High y^+ wall treatment is the classic wall-function approach, where wall shear stress, turbulent production and turbulent dissipation are all derived from equilibrium turbulent boundary layer theory. It is assumed that the near-wall cell lies within the logarithmic region of the boundary layer, therefore the centroid of the cell attached to the wall should have $y^+ > 30$.

The low y^+ wall treatment assumes that the viscous sublayer is well resolved by the mesh, and thus wall laws are not needed. It should only be used if the entire mesh is fine enough for y^+ to be approximately 1 or less. The all y^+ wall treatment is an additional hybrid wall treatment that attempts to combine the high y^+ wall treatment for coarse meshes and the low y^+ wall treatment for fine meshes. It is designed to give results similar to the low y^+ treatment as $y^+ < 1$ and to the high y^+ treatment for $y^+ > 30$. It is also formulated to produce reasonable answers for meshes of intermediate resolution, when the wall-cell centroid falls within the buffer region of the boundary layer, i.e. when $1 < y^+ < 30$.

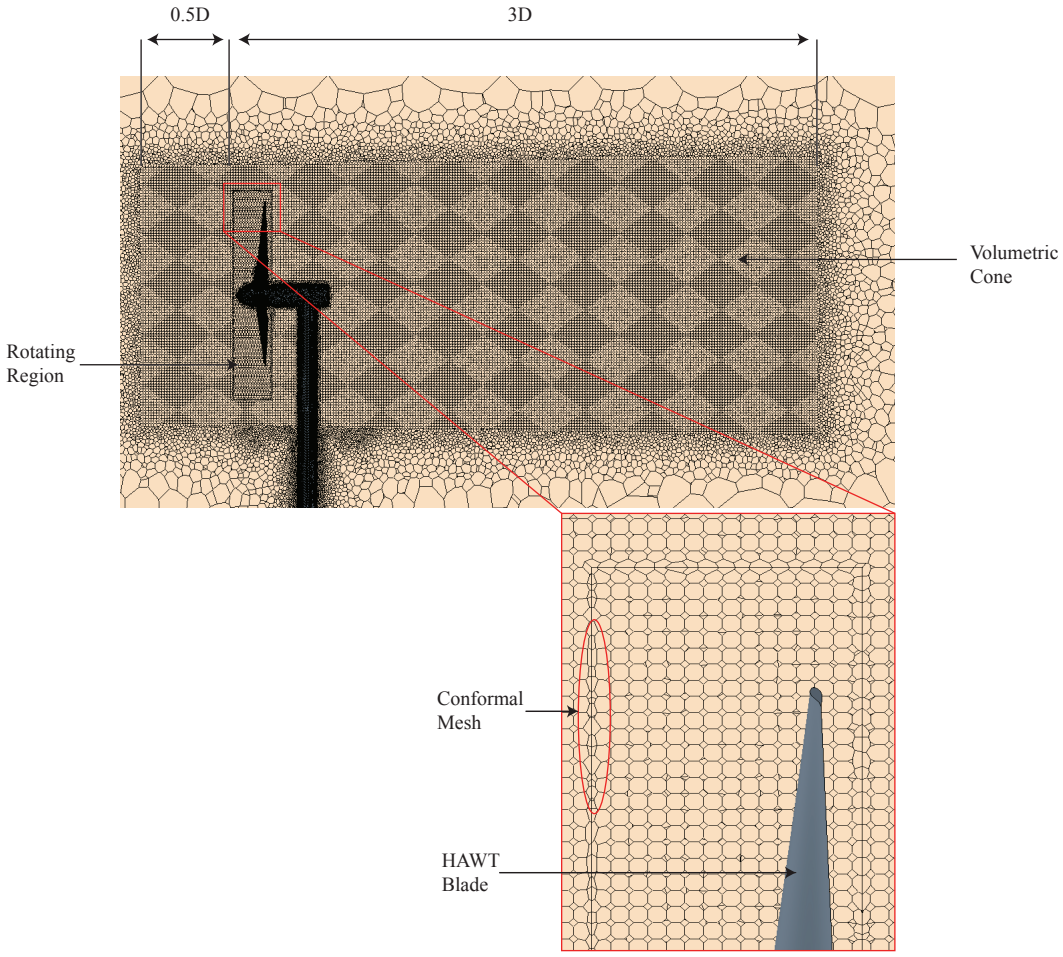

Figure 7: Meshed solution domain showing volumetric wake cone and conformal mesh across region interfaces

The use of these treatments is dependant on the y^+ values over the geometry where y^+ is a non-dimensional wall-normal distance, defined as:

$$y^+ = \frac{yu^\star}{\nu} \tag{12}$$

where y is the normal distance from the wall to the wall-cell centroid. The term $u^\star$ is a reference velocity and ν is the kinematic viscosity. The reference velocity is related to the wall shear stress as follows:

$$u^\star = \sqrt{\tau_w/\rho} \tag{13}$$

where τ_w is the wall shear stress and ρ is fluid density.

For this study, the y^+ value over the blades was kept below a value of 1 (maximum ≈ 0.67) during simulation initialization in order to accurately resolve the boundary layer flow (figure 8) [46]. However, for a rotating component (the blades in this case) the y^+ values can change. The magnitude of this change has not been noted in previous CFD investigations reviewed by O'Brien et al. [5]. Changing y^+ values has a direct impact on the selected wall treatment used. In this case, the increasing tangential velocity value of the blade towards the blade tip altered the y^+ values. It is difficult to assess beforehand what the maximum y^+ over the blade will be during simulation. Blade y^+ values were monitored during initial simulations with the selected mesh density (outlined in section 3.6). Figures 9a and 9b show the average and maximum y^+ values of a blade after several rotor rotations for a TSR value of 2.54. It can be seen that peak y^+ values above 1 are recorded; therefore, an all y^+ wall treatment was used in the current study. Similar trends were monitored for the TSR equals 3.87 case. Additionally, y^+ values over the tower varied in the range of $0.29 < y^+ < 8.87$, with a considerable amount of the tower structure falling into the buffer region. This again prompted the use of an all y^+ wall treatment. Correct selection of y^+ wall treatments is required to accurately model the boundary layer near a wall. An incorrectly selected wall treatment would result in an inaccurately predicted velocity gradient at the wall and therefore inaccurate predictions of velocity and turbulent characteristics.

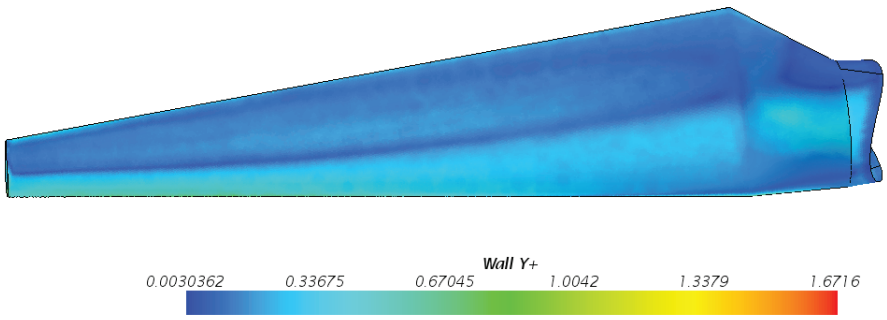

Figure 8: Y^+ values over numerical turbine blade (TSR 2.54)

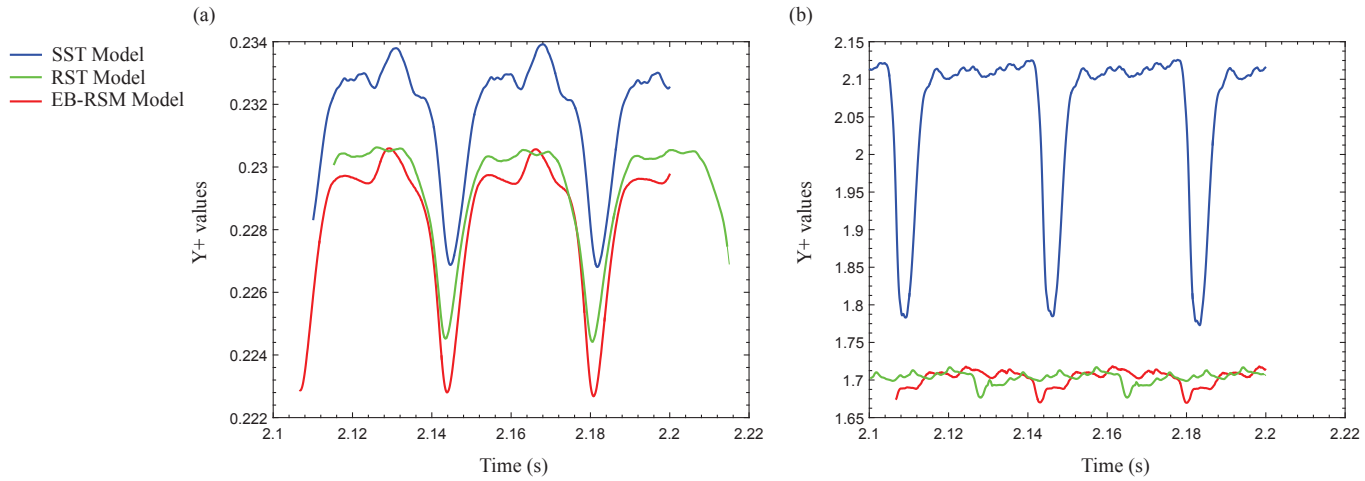

Figure 9: Varying Y^+ values over numerical turbine blade for average Y^+ (a) and maximum Y^+ (b) values (TSR 2.54)

4. Results and Discussion

4.1. Introduction

This section presents the results of the experimental investigation of the wake behind a model horizontal axis wind turbine in comparison to numerical predictions. The results are divided into three main sections: the mean velocity characteristics of the wake, turbulence characteristics of the wake and assessment of current modelling approaches. All results are presented from an upstream position, for a freestream velocity of 10 m/s. Two tip speed ratios (TSRs) were investigated (i.e. 2.54 and 3.87). TSR 2.54 represented the turbine operating at its optimum TSR. TSR 3.87 represented the turbine operating above its optimum TSR value. All graphs are normalized against the model turbine radius with Z/R equals 0 representing the centre of the rotor. The axial velocity profile in the wake is presented in a non-dimensional format U_x/U_∞, where U_x is the streamwise velocity at the plane and U_∞ is the freestream velocity. Data is taken from a horizontal line through the middle of the rotor at three separate locations downstream (0.66D, 1D and 1.5D).

A number of volume renders from CFD solutions will be presented. Because the flow is time dependant, the results discussed in this section represent a statistical average of the flow field for a large amount of rotor rotations.

Firstly, the mean velocity deficit behind the rotor for both TSR cases is compared to numerical predictions. Accurate predictions of the wake velocity deficit would confirm that the numerical models were able to accurately model rotor loading and the momentum deficit created by the extraction of energy from the flow by the HAWT.

The ability of each model to predict turbulence characteristics of the wake is also investigated. With respect to future wind turbine structural modelling attempts, an understanding of the spatial distribution of stresses generated within the wake is important. Additionally, understanding the limitations of turbulence models to predict stresses in the flow is important as this would impact on the choice of modelling strategy used in future FSI simulations. Turbulence plays a direct role on the unsteady forces and bending moments experienced by turbine blades downstream. Additionally, a comprehensive understanding of the turbulent characteristics of a turbine wake are necessary for validating and guiding the development of sub-grid scale parameterizations in high fidelity numerical models such as LES [10]. The $\overline{u'v'}$ Reynolds stress component is normalized by the square of the freestream velocity U_∞^2 and is presented against the non-dimensional distance Z/R.

4.2. Mean Velocity Characteristics

From the offset, it can be seen that there is good agreement between the experimental and computational results. A strong correlation is observed between figures 10a, 10b and 10c in terms of velocity deficit for a TSR value of 2.54. Both numerical and experimental results show the velocity deficit takes the form of a Laplace distribution. Experimental data shows a severe decrease in axial velocity, particularly around the region Z/R = 0, which corresponds to the region directly behind the hub of the model wind turbine. All numerical models predict similar results with average percentage errors between numerical and experimental results ranging between 2–4%. The ability of each turbulence model to accurately capture wake velocity deficit confirms that the numerical models were able to accurately model rotor loading and the momentum deficit created by the extraction of kinetic energy from the flow by the HAWT.

If the centre of the wake is defined as the point where the velocity deficit was maximum, then as shown in figures 10a, 10b and 10c, the point of maximum recorded velocity deficit in the wake is located at Z/R = 0.1. In figures 11a, 11b and 11c (which present contour plots of experimentally recorded axial velocity), the centre of the wake tends to drift slightly down to the right at Z/R= 0.1 and Y/R = -0.12 with minimum values of $0.33U_\infty$ at 0.66D and $0.64U_\infty$ at 1.5D. This could be attributed to the pressure field around the turbine. For explanation purposes, the root vortex system is compared to the tip vortex of a simple wing. In flight, a pressure differential exists at the tip of a simple wing, which results in airflow rotating around the wing tip from the high to low pressure region. Similarly, a low pressure region exists behind the turbine, below the nacelle structure, due to the presence of the tower structure. There is less obstruction to the wake in the upper region, which leads to higher pressure values in the upper wake region, relative to the lower part of the wake. The combination of high and low pressure regions may result in the centre of the wake drifting downwards towards the low pressure region. Now, considering the simple wing case, the movement of the airflow around the wing tip causes the tip vortex to move inboard [47]. Again, for the current study, the HAWT is rotating in an anti-clockwise direction. This applies a torque to the wake, which results in a clockwise rotating wake and therefore a

clockwise rotating root vortex system. This, would result in the root vortex system drifting outboard towards the right, which results in a wake centre that is off centre and to the right of the nacelle/tower structure.

Velocity deficit values are seen to concentrate behind the hub structure (figures 11a, 11b and 11c). The velocity deficit extends 0.5R, which would suggest that the root vortex system and the turbine structure are the major contributors to the wake velocity deficit, as shown in figure 11. However, beyond 0.5R the velocity deficit is seen to recover rapidly, which contradicts previous studies. The wake is usually defined by a reduced velocity value where the recovery of the wake to freestream values usually occurs near the edge of the rotor as shown in a study carried out by Schüemann et al. [48]. This is possibly due to the aerofoil design used. The rotor blades featured a FFA-W3-241 aerofoil (as indicated in section 2.2). Originally designed at FFA (The Aeronautical Research Institute of Sweden); the aerofoil has a relatively high thickness at 21% and is typically used on the inboard sections of turbine blades [49], however, the aerofoil is not suitable for use at the outboard sections of the blade, which would result in low rotor loading towards the rotor edge. However, the data taken in this study allows us to see that the tower structure, nacelle and the central root vortex system supply a constant velocity deficit to the wake. Additionally, the close comparison of numerical and experimental data makes the current study suitable for turbulence model validation as the characteristics of the FFA aerofoil are known. This is supported by Vermeer et al. [18], who stated that as long as the characteristics of the aerofoil are known, the aerofoil is suitable for turbulence model validation.

The outer regions of the rotor blades do reduce the freestream velocity behind the rotor, but it is noticeable only when data is recorded over a large period of time, as shown in figure 12 (where mean velocity deficits in the wake range predominantly from 66% of freestream values for TSR equals 2.54). Once outside the influence of the turbine structure and thicker blade roots, the velocity in the outer regions of the rotor is only periodically reduced as opposed to continuously experiencing a constant velocity deficit. The influence of the blades on the wake velocity deficit towards the rotor edge becomes smaller as the blade chord length decreases. Thus, there is a return to freestream velocity values due to reduced rotor solidity (and low blade loading), particularly in the other most region of the wake (as seen for TSR 2.54 in figure 12). In addition, the large nose cone generates a considerable velocity reduction (up to $0.7U_\infty$) in front of the rotor, as shown in figure 12, which would also aid the wake velocity deficit in the region close to the wake centre. This aspect of model design has not been mentioned in previous studies outlined in a review by O'Brien et al. [5] and should be considered for future works on this topic. The nose cone design used has a great impact on the formation of the wake, particularly the centre of the wake structure as flow over the nose cone alters flow over the blade roots and therefore alters the structure of the central vortex system of the HAWT wake. In the current study the wake structure is defined by a velocity deficit generated by the central root vortex system and the tower/nacelle structure. This central system is surrounded (seen on the upper half of the wake outside the influence on the turbine structure in figure 12A) by a region of fluid moving at freestream velocity.

Outside this again, the presence of the tip vortex region can be identified as the region with slightly reduced velocity values of $0.95U_\infty$.

Towards the blade tip region (Z/R = $\pm$1), as shown in figure 10, all models tend to over predict velocity values in this region. There are several possible reasons for this. Firstly, when considering the SST $k-\omega$ model, the increase in velocity at Z/R = $\pm$1 could be a result of under-estimation of vortex diffusion and the prediction of a more tightly bound tip vortex. This could be a result of the dense wake mesh used (outlined in section 3.6), combined with the Vorticity Confinement Model. Typically the Vorticity Confinement model is used to reduce the mesh density of a simulation and maintain a vortex structure by the addition of a forcing term (outlined in section 3.2). However, the very dense mesh in the wake region would already have minimized the dissipation of the tip vortices. This combined with the Vorticity Confinement Model would have further reduced vortex dissipation, which would explain the under-estimation of the diffusion of the tip vortices (resulting in a stronger vortex) and the increase in axial velocity in the tip region. Noted by Anderson et al. [50], an increase in vortex strength can result in an increase in axial velocity in the core of a tip vortex. This relationship between core axial velocity and vortex strength was also seen by O'Regan et al. [51]. Following this, a study by O'Regan et al. [47] recorded that stronger vortices also have increased axial velocity values in the vicinity around them, which would explain the increased axial velocity values at the tip region in the current study.

Regarding the RST model, the turbulent dissipation rate is obtained from a transport equation analogous to the $k-\epsilon$ model. As described by Menter [52], in the standard $k-\epsilon$ model, eddy viscosity is determined from a single turbulence length scale; whereas, in reality all scales of motion will contribute to the turbulent diffusion. The same process is used for the EB-RSM model. This could have contributed to the under-estimation of the diffusion of the tip vortices and lead to the same result as outlined above.

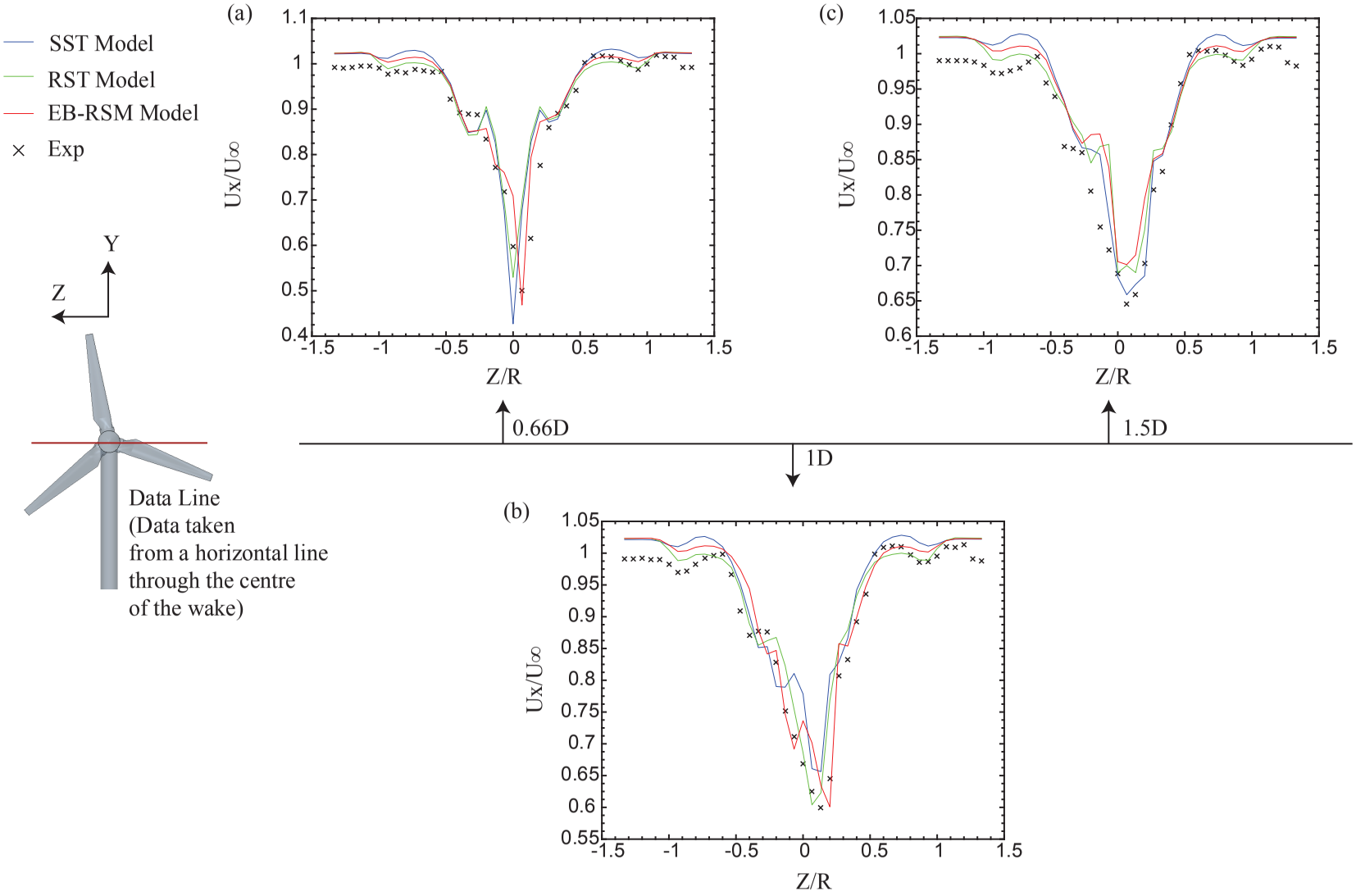

Figure 10: Axial velocity deficit values for a TSR value of 2.54

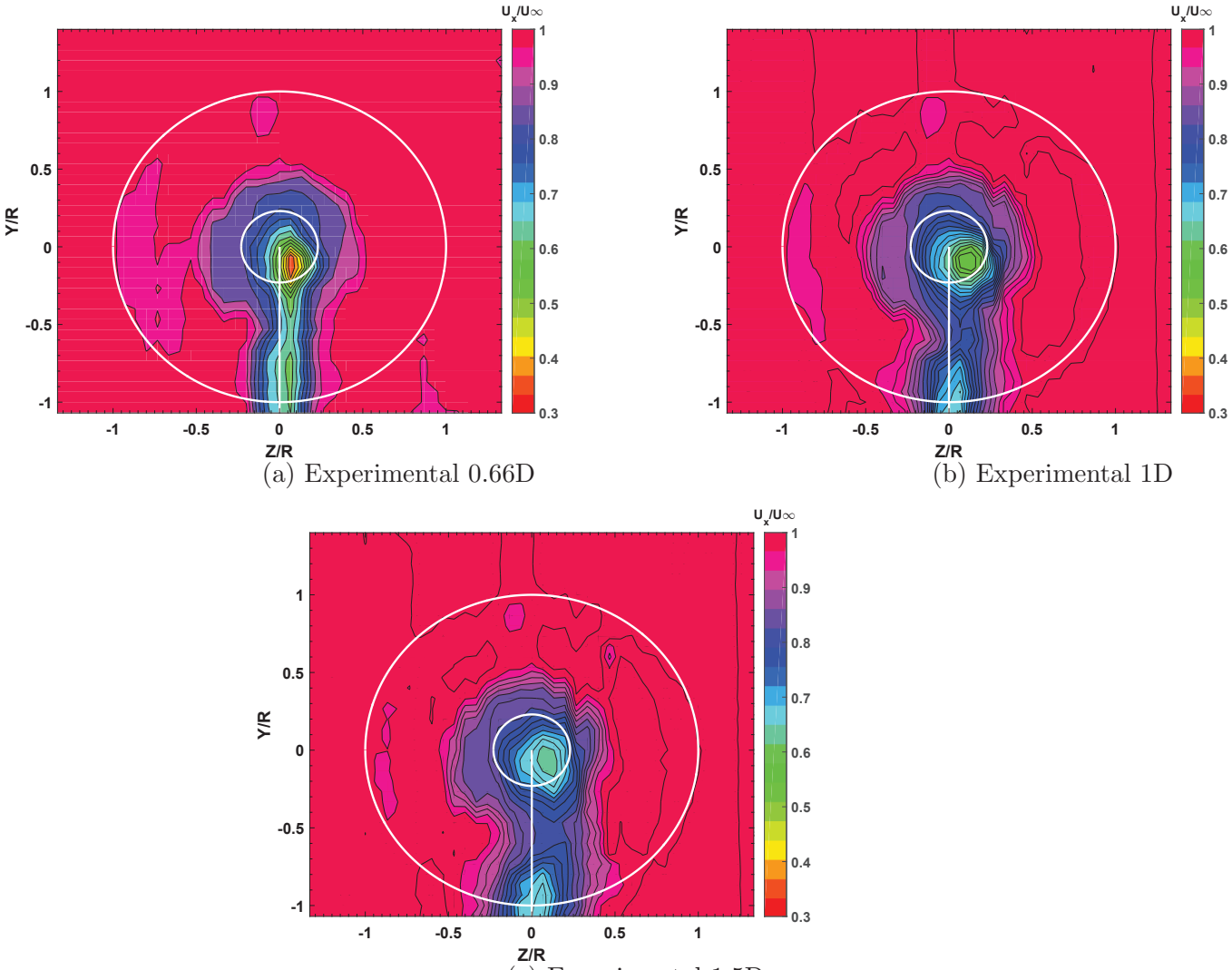

(a) Experimental 0.66D

(b) Experimental 1D

(c) Experimental 1.5D

Figure 11: Plots of axial velocity shown 0.66D, 1D and 1.5D downstream for TSR = 2.54

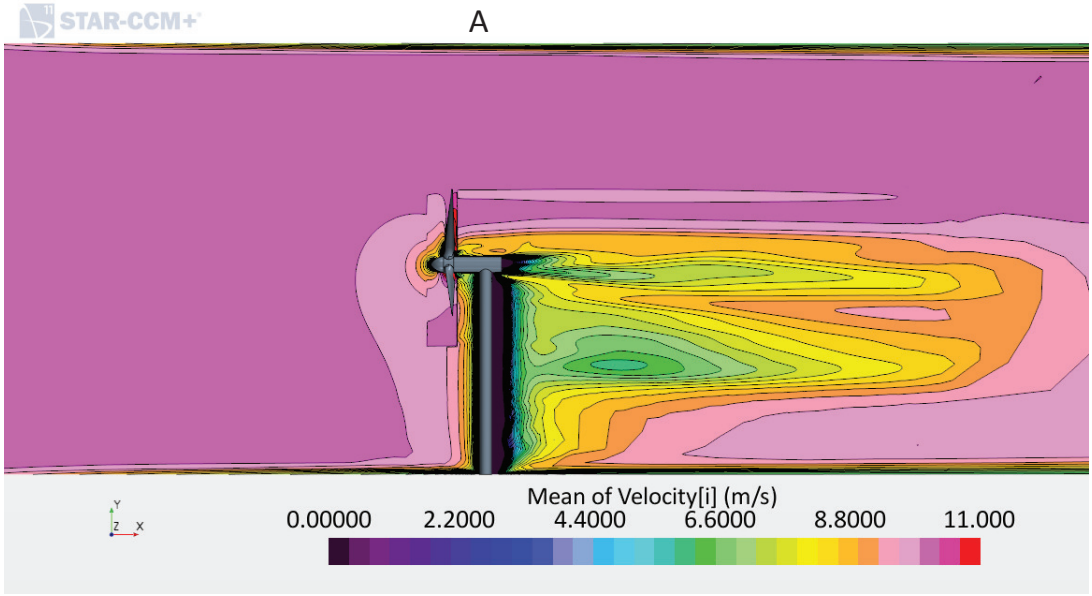

Figure 12: Mean axial velocity distribution within the HAWT wake for TSR = 2.54 predicted by RST simulation

From a qualitative point of view, the ability of the numerical models to capture the root vortex system and central velocity deficit in the wake has been attributed to the dense measurement grid and the thick aerofoil section used with a sharp taper towards the root section, creating distinct root vortices as shown in figure 13 . Due to their compact propagation downstream and the strength of the root vortices, they appear to form a vortex sheet, with its formation attributed to the root vortices shedding from each blade. This formation has previously been described by Gømez-Elvira et al. [53] and Sanderse [17], but only in terms of the tip vortices. A volume render of the turbine wake is shown is figure 13, with the scaler range adjusted to promote viewing of the described central vortex. As seen in the volume render of figure 13, the central vortex does not fully develop until approximately 1.5D to 2D downstream. This was seen in all the numerical models. The individuality of each root vortex persisted longer downstream than experimental results. This again was attributed to the numerical models under-estimating vortex diffusion.

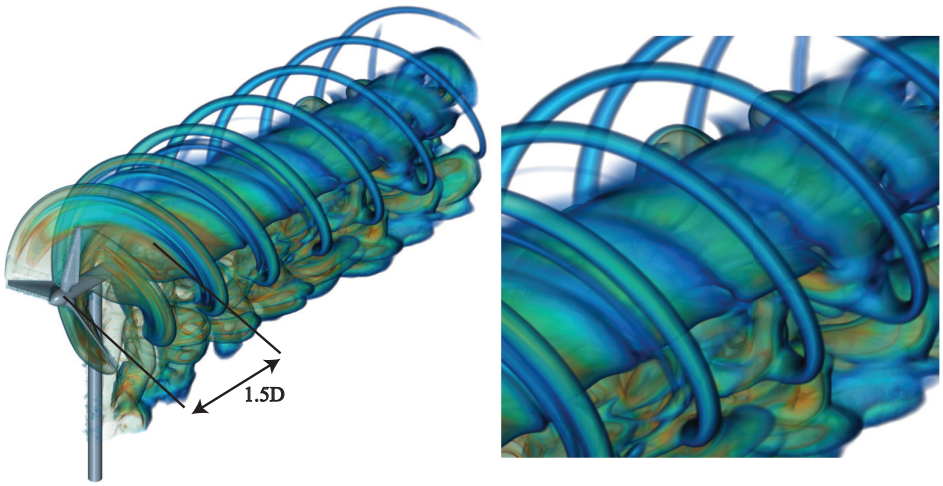

Figure 13: Volume render from RST simulation showing central vortex sheet. TSR = 2.54

Figure 14 shows the comparison between numerically predicted and experimentally recorded velocity deficit in the wake for a TSR value of 3.87. Similar to results for a TSR value of 2.54, there is good agreement between numerical and experimental results. The velocity deficit takes the form of a Laplace distribution, which is typical of HAWT models. Experimental data shows the largest velocity deficit occurred at Z/R = 0.1, similar to TSR equals 2.54. Maximum (experimentally recorded) axial velocity deficit behind the rotor is $0.51U_\infty$ at 0.66D and recovers to $0.67U_\infty$ at 1.5D. Average percentage errors between numerical and experimental results ranged between 4–7%.

Similar to experimental results for TSR value of 2.54, the centre of the wake is slightly right of centre as shown in figures 15a, 15b and 15c. Here, minimum values of $0.4U_\infty$ at 0.66D and $0.69U_\infty$ at 1.5D are recorded.

It is noted that in experimental data shown in figures 15a, 15b and 15c that the deficit created by the tips almost completes 360°. This velocity deficit forms a complete circular pattern in experimental plots where TSR equals 3.87. This would suggest that the angle of the helical path of the wake, given by the flow angle at the blade tip, is inversely proportional to the tip speed ratio [11]. Similar to experimental results for TSR equals 2.54, the nacelle and tower structure had the greatest influence on the velocity deficit behind the turbine structure. A larger velocity deficit was noted when the turbine operated at a TSR value of 2.54. This was the optimum operating condition for the HAWT model and therefore the maximum quantity of kinetic energy was extracted from the flow. The wake recovers slower for the TSR equals 2.54 case with a velocity deficit of $0.64U_\infty$ recorded in the centre of the wake at 1.5D downstream. At the same location for TSR equals 3.87, the velocity deficit value was $0.69U_\infty$. Common to both TSR cases, the velocity deficit recovers faster in the region behind the tower, which could be attributed to the enhanced mixing in the area due to a combination of both the tower and rotor wakes. There are two concentrated areas of

reduced velocity in figure 15c. These are defined by the authors as spurious data points and should be ignored.

Considering the velocity deficit profile for the TSR equals 3.54 case, it is clear that there is an increase in velocity at Z/R = ±0.6 (figure 14). This was attributed to the location of a secondary vortex structure. The secondary vortex structure formed between 55% and 65% of the blade span and resulted in an increase in the wake velocity to $1.07U_\infty$. The structure merged with the tip vortex system and complete decay of the secondary structure occurred at 2D downstream. A similar secondary structure was noted by Yang et al. [11] and Whale et al. [6]. The structure formed between 50% and 60% of the blade span in the study carried out by Yang et al. [11] and merged with the tip vortex system at 1D downstream. A similar structure recorded by Whale et al. [6] merged with the tip vortex system at 1D downstream. Figure 16 shows the flow over the suction surface of one of the turbine blades for both TSR values. At the lowest TSR value of 2.54, it can be seen that the flow remains mostly attached with minor separation beginning at the trailing edge. The flow is heavily influenced by centrifugal effects with flow in the radial direction most dominant. At TSR equals 3.87, a large area of separation occurs around 56% blade span, which coincides with the presence of the secondary vortex structure. Again, all numerical models over predicted the axial velocity in the wake at Z/R = ±0.6, which, as outlined earlier, could be a result of each turbulence model over-estimating vortex strength and possibly under-estimating turbulent-diffusion.

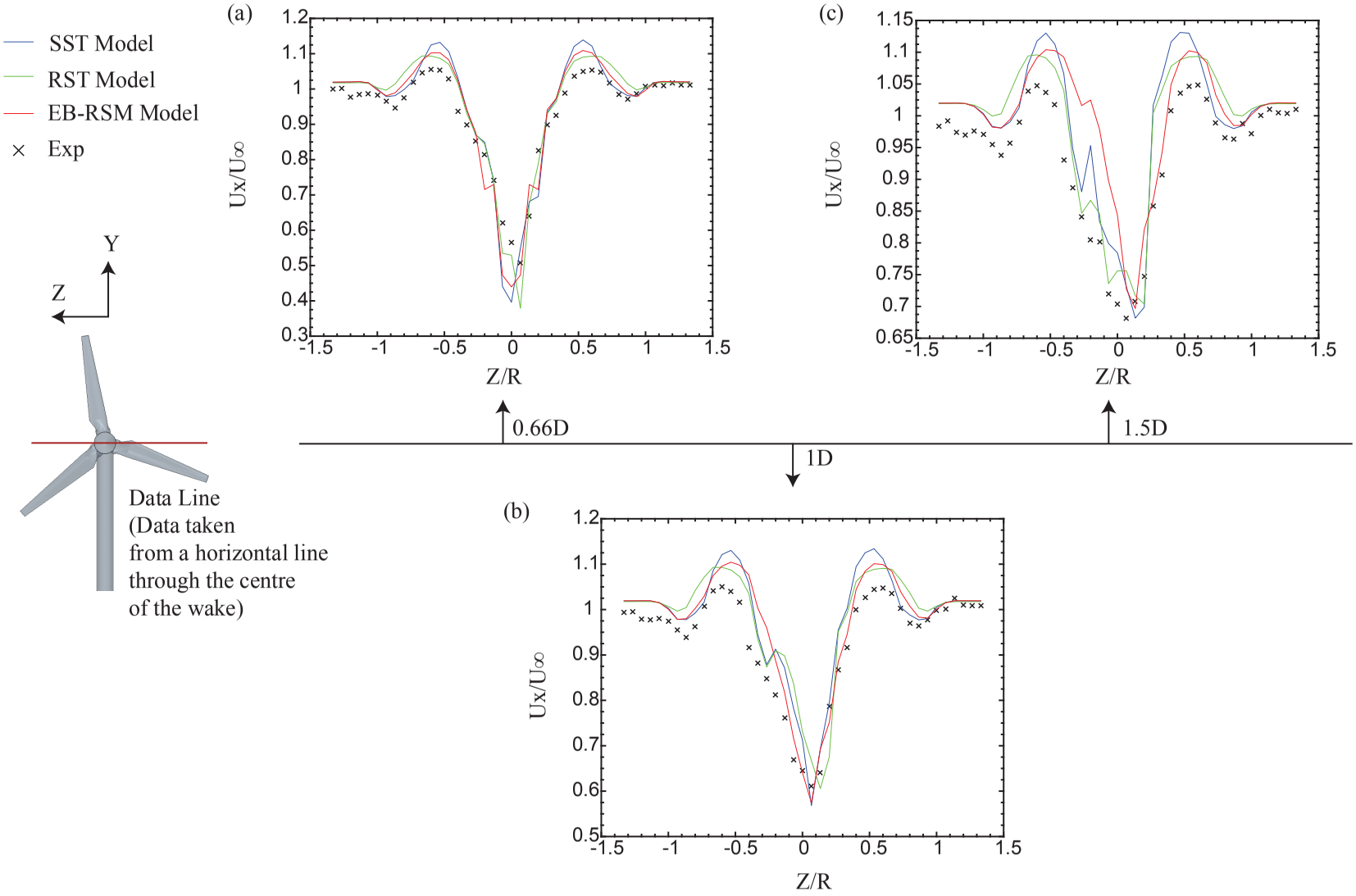

Figure 14: Axial velocity deficit values for a TSR value of 3.87

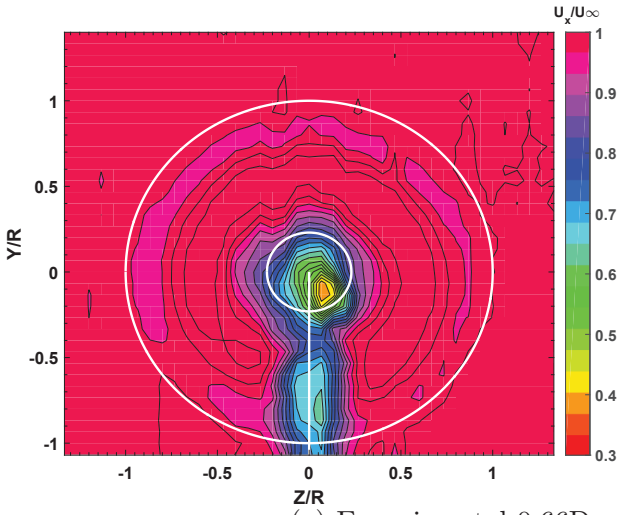

(a) Experimental 0.66D

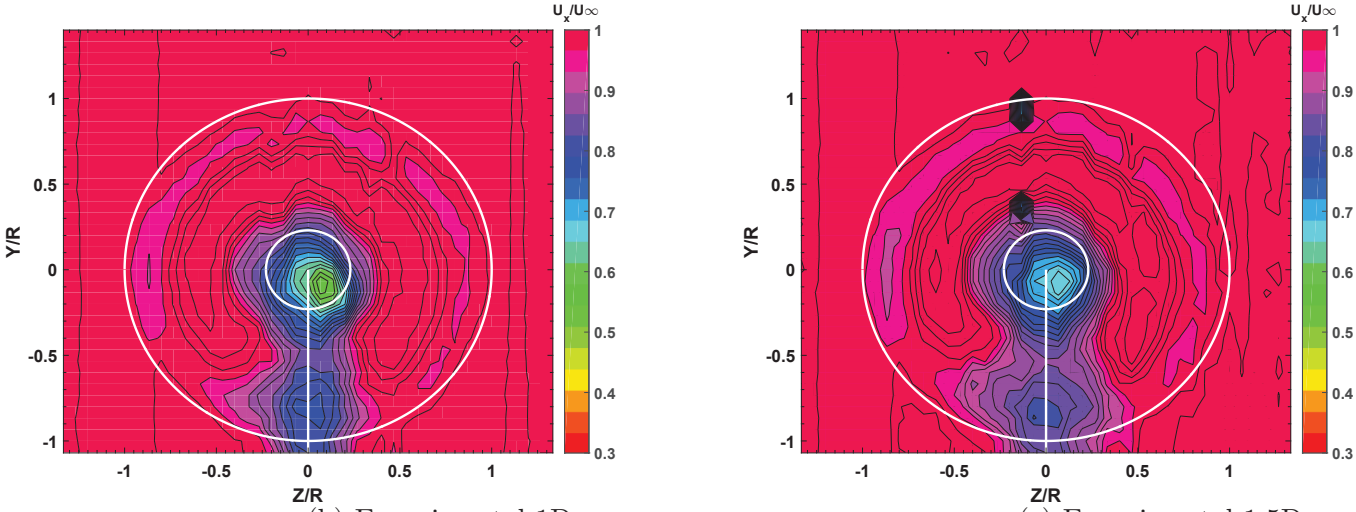

(b) Experimental 1D

(c) Experimental 1.5D

Figure 15: Plots of axial velocity shown 0.66D, 1D and 1D downstream for TSR = 3.87

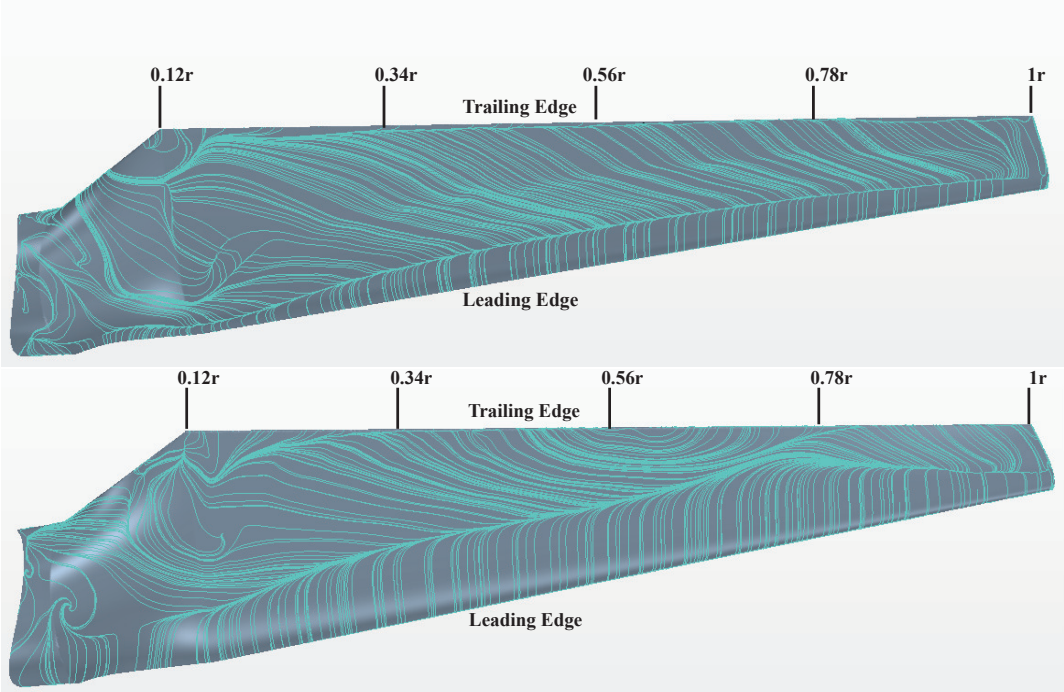

Figure 16: Streamlines on the surface of a computational blade at TSR = 2.54(top) and 3.87(bottom)

4.3. Turbulence Characteristics – Time averaged u' and v' velocity components

As outlined in section 4.2, peak velocities near the blade tip and root regions for TSR values of 2.54 and 3.87 respectively have been attributed to turbulence models over-predicting vortex strength and under-estimating turbulent diffusion. Under-estimating turbulent diffusion, which would result in a more stable and stronger vortex system, arises from the under-prediction of fluctuating components in the flow. Under-predicting fluctuating velocity components and Reynolds stresses in the flow reduces the mixing rate within the wake and therefore, wake structures such as tip and root vortices can be preserved in the wake. Additionally, the wake itself is preserved further downstream. With respect to future wind turbine structural modelling attempts, an understanding of the spatial distribution of stresses generated within the wake is important. The fluctuating velocity components in the flow directly contribute to the unsteady forces acting on turbine blades.

To understand the ability of each turbulence model to predict the turbulent characteristics of a HAWT wake, both the Reynolds stress values and the Root Mean Squared (rms) values of both the u' and v' fluctuating velocity components were investigated. This gave an appreciation of the ability of each turbulence model to predict the magnitude of the fluctuating velocity components in the wake.

Figures 17 and 18 show the normalized rms velocity fluctuations for the u' velocity component at different locations downstream for both TSR values. Considering figure 17 (which

shows the rms u' values for TSR equals 2.54), it can been seen that there is good agreement between numerical and experiment results. All numerical models predicted the magnitude of the rms u' velocity component to the correct order of magnitude. However, at all downstream locations, all numerical models under-predicted the rms u' component in the wake near the blade tip region Z/R = $\pm$1 with the exception of the RST model at 0.66D. All models under-predicted the rms u' component in the centre of the wake around Z/R = 0, with the exception of the EB-RSM model at 1D downstream and both the SST $k-\omega$ and EB-RSM model at 1.5D downstream. Both experimental and numerical data show the rms u' velocity component take the form of an inverse Laplace distribution. For TSR value of 2.54 (figure 17), experimentally recorded peak rms u' velocities consistently occur at Z/R = 0.1, which coincides with the centre of the wake as mentioned in section 4.2. Interaction between the central root vortex system and the turbine structure leads to enhanced mixing in this region. Maximum values of 0.12, 0.1 and 0.08 were recorded at 0.66D, 1D and 1.5D, respectively. The decreasing values of rms u' in the centre of the wake appear to descend linearly for a TSR value of 2.54 and illustrate the reduction of wake turbulence with distance downstream. Additional peaks are also present at Z/R = $\pm$1 at each measurement location downstream, which coincides with the blade tip location. Maximum values of 0.025, 0.0225 and 0.0212 were recorded at 0.66D, 1D and 1.5D, respectively. This again shows a near linear reduction of rms u' values in the blade tip region.

Each numerical model appeared to have both advantages and disadvantages associated with them. Across all measurement planes in figure 17, the RST model tended to most accurately predict rms u' values in the blade tip region Z/R = $\pm$1, with percentage errors ranging from -15% to +17% (the RST model under-predicted the rms u' values at every measurement plane with the exception at Z/R = -1 at 0.66D) of experimental results over 1.5D downstream. Both the SST $k-\omega$ and EB-RSM model consistently under-predicted rms u' values in the blade tip region with percentage errors ranging from -3% to -34% of experimental results over 1.5D downstream. Regarding the blade tips at Z/R = $\pm$1 for TSR value of 2.54, in this region each turbulence model consistently under-predicts the rms u' velocity component. The under-prediction of rms u' in this region would support the argument made in section 4.2 that all models under-predicted vortex diffusion, turbulent dissipation and overall turbulent instability in this region. All models were more consistent regarding the prediction of rms u' values in the region Z/R = 0. Here the EB-RSM model tended to predict the highest levels of rms u' values in the wake, with the RST model consistently predicting the lowest. At Z/R = 0.1, the percentage difference between numerical and experimental results were -8%, -43% and -7% for the SST $k-\omega$, RST and EB-RSM models respectively at 0.66D. With distance downstream, the RST model tended to more closely resemble experimental results at Z/R = 0.1 with the percentage difference between experimental results and the RST model being -26% at 1.5D. However, at this point both the SST $k-\omega$ and EB-RSM model over-predicted experimental results by 34% and 61%. Although experimental results show a linear reduction of peak rms u' values in the wake centre, none of the numerical models followed this trend.

Similar results are seen in figure 18, which shows the distribution of the rms u' velocity component for a TSR value of 3.87. Peak rms u' velocities are located at Z/R = 0.1 (again the location of the wake centre). Immediately, it can be seen in figure 18a that all numerical models greatly under-predicted the rms u' velocity component. This trend continued with distance downstream. Maximum values of 0.107, 0.1 and 0.08 were recorded at 0.66D, 1D and 1.5D, respectively for experimental results at Z/R =0.1. The RST model greatly under-predicted the magnitude of the rms u' velocity component. The RST model tended to predict fluctuating rms u' velocities around 0.03 through most of the centre of the wake, which suggests that the model predicted less shedding across the rotor. An increase in u' velocities are located at Z/R = $\pm$0.8, which are caused by the secondary vortex mentioned in section 4.2. Here peak experimental rms u' values are 0.037, 0.035 and 0.032 at 0.66D, 1D and 1.5D, respectively. Similar to peak rms u' velocities in the wake centre for TSR value of 2.54, the rms u' velocities for the secondary vortical structure appear to decrease linearly with distance downstream. Again, all turbulence models under-predicted rms u' values in this region.

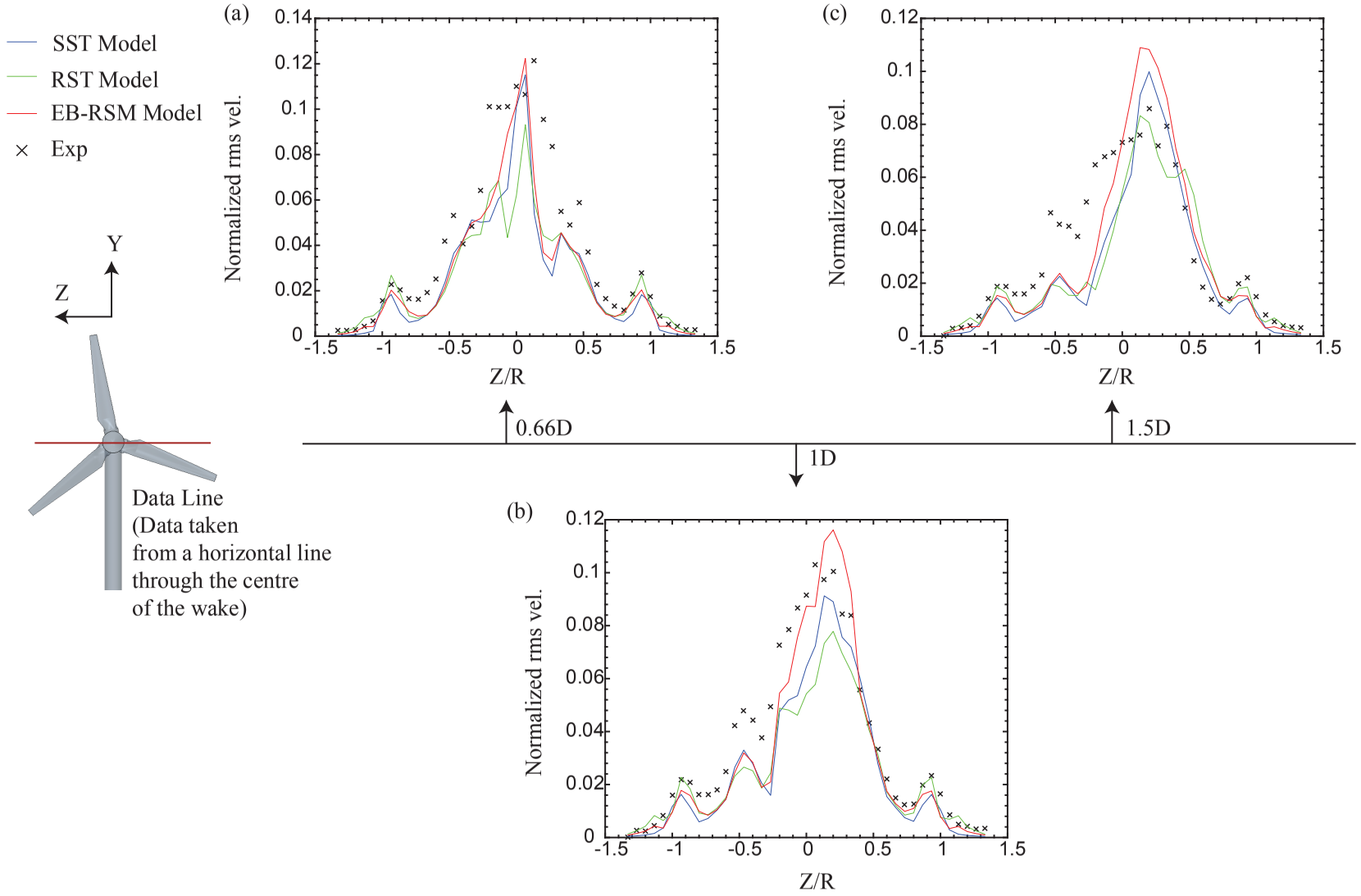

Figure 17: Normalized rms velocities $\frac{\sqrt{\overline{u'^2}}}{U_\infty}$ at 0.66D (a), 1D (b) and 1.5D (c) downstream for TSR equals 2.54

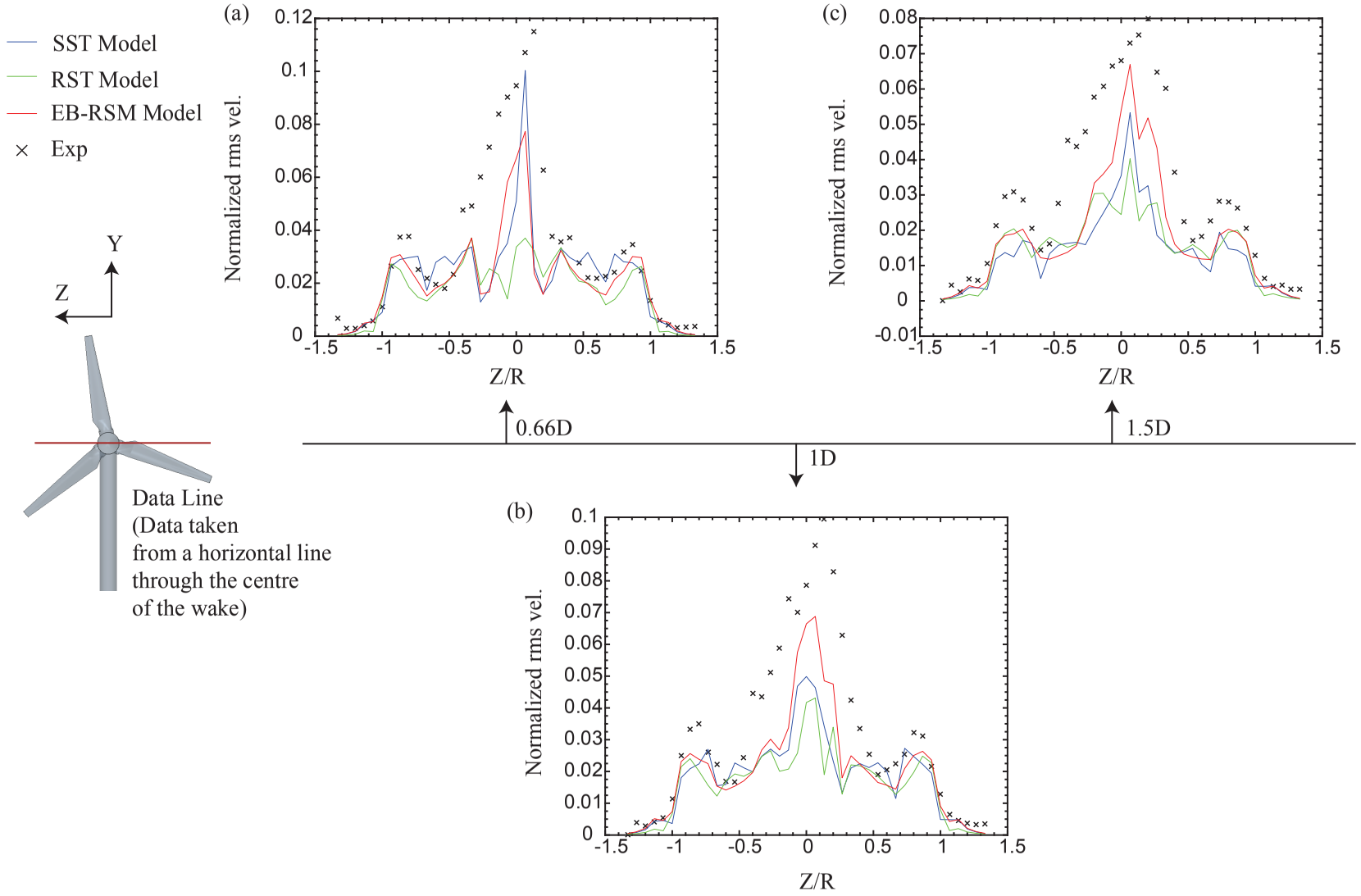

Figure 18: Normalized rms velocities $\frac{\sqrt{\overline{u'^2}}}{U_\infty}$ at 0.66D (a), 1D (b) and 1.5D (c) downstream for TSR equals 3.87

Figures 19 and 20 show the rms velocity fluctuations for the v' velocity component at different locations downstream for both TSR values. Again, the experimental rms v' values in the wake take on an inverse Laplace distribution. Maximum experimentally recorded rms v' values occur at Z/R = 0.1 for both TSR cases, similar to those recorded for the TSR equals 2.54 case. However, unlike the TSR 2.54 case, peak experimental rms v' values tend to stay the same with distance downstream with values of 0.101, 0.104 and 0.101 at 0.66D, 1D and 1.5D, respectively downstream for a TSR value of 2.54. Peak rms v' values of 0.09, 0.09 and 0.075 were recorded at 0.66D, 1D and 1.5D, respectively downstream for a TSR value of 3.87 (figure 20). Additionally, peak rms v' values occur at Z/R = $\pm$0.7, the location of the secondary vortex for a TSR value of 3.87. Here peak experimental values of 0.032, 0.032 and 0.029 are recorded at 0.66D, 1D and 1.5D downstream. Comparison of the peak experimental rms u' and rms v' values for both TSR cases highlight that both velocity components are similar in magnitude, with the rms v' magnitude on average being 95% of the rms u' values.

Similar to the predicted values of rms u', all turbulence models predicted the magnitude of the rms v' components to the correct order of magnitude for both TSR cases. However, all models tended to over-predict rms v' components from Z/R = $\pm$0.5 and outward towards the blade tip for both TSR equals 2.54 and 3.87 (figures 19 and 20).

The models for the most part under-predicted the rms of the fluctuating velocity components, in particular for TSR equals 3.87 in the region Z/R = 0. This was attributed to varying y+ distributions over the blades, which increased the difficulty for the models to resolve the boundary layer. In addition to this, increased velocities at the high TSR value would have altered the y+ values present over the nacelle even further. This would have further reduced the resolution of the boundary layer over the nacelle for the TSR = 3.87 case. The larger inaccuracies towards the Z/R = 0 region is attributed to the fact that the y+ values over the nacelle are the same as the values specified for the tower structure. Therefore, shedding from the nacelle structure itself would not have been resolved for to the same accuracy as that of the blades. As noted by Sanderse [17] the root vortices are in close proximity to each other. This, combined with the induced turbulence from the turbine structure, cause the root vortices to be destroyed much earlier than the tip vortices. Sherry et al. [28] attributed the interaction between the nacelle boundary layer and the root vortex as a component in the root vortices early destruction. This is because the vorticity created within the nacelle boundary layer is of the same order of magnitude and opposite in sign to the coherent root vortices, resulting in cross-annihilation of vorticity between the root vortex and the nacelle boundary layer.

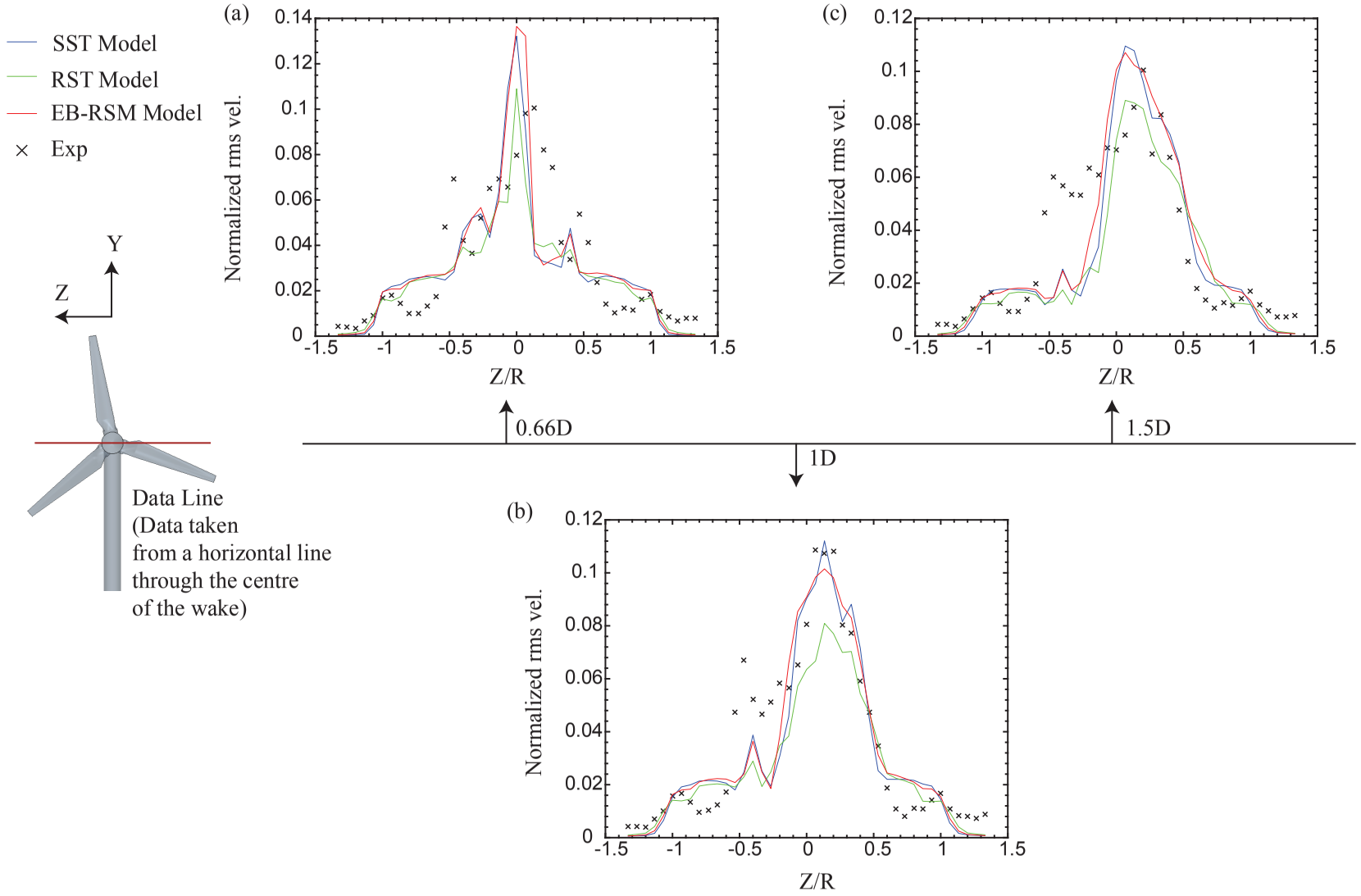

Figure 19: Normalized rms velocities $\frac{\sqrt{\overline{v'^2}}}{U_\infty}$ at 0.66D (a), 1D (b) and 1.5D (c) downstream for TSR equals 2.54

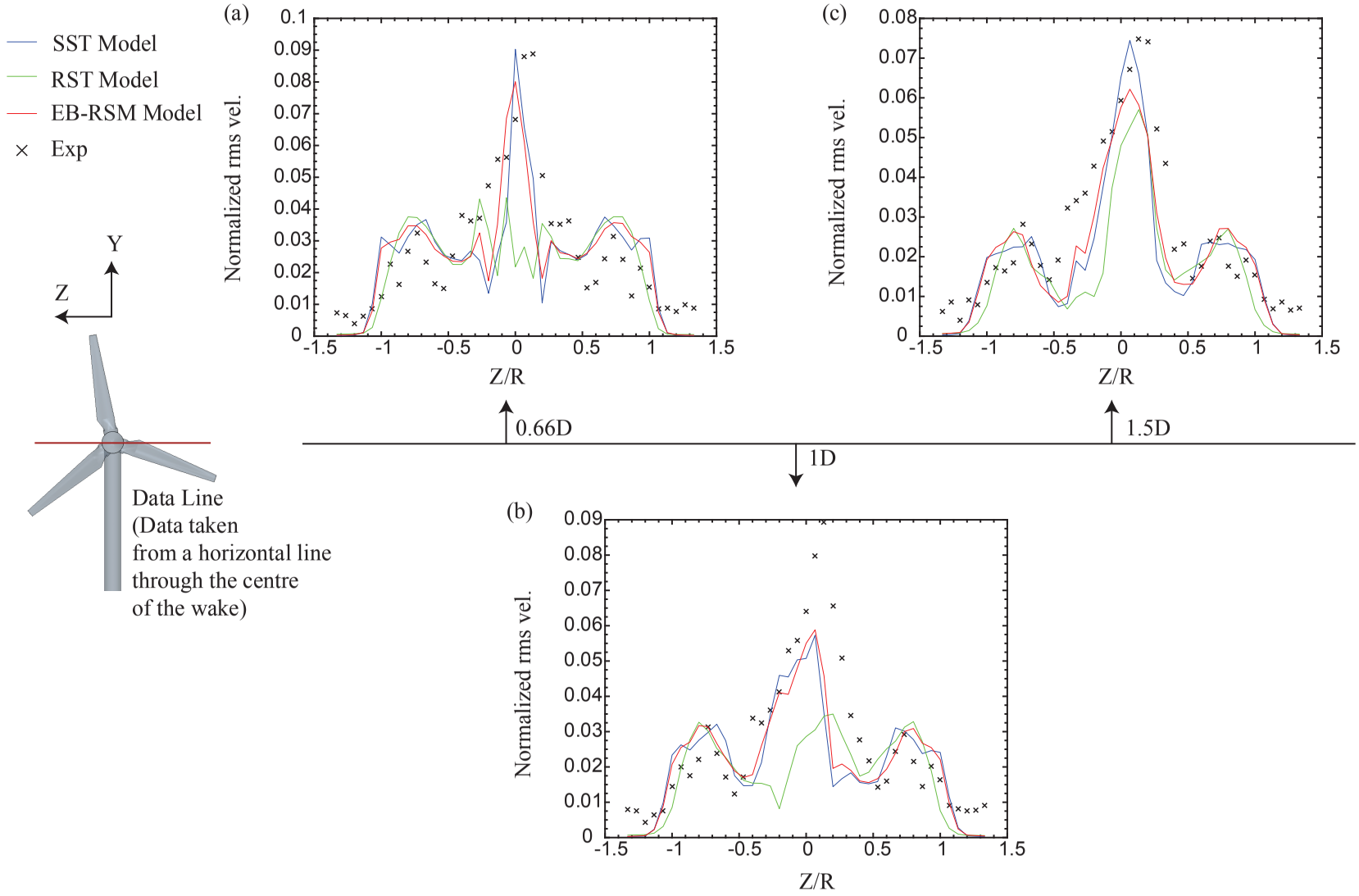

Figure 20: Normalized rms velocities $\frac{\sqrt{\overline{v'^2}}}{U_\infty}$ at 0.66D (a), 1D (b) and 1.5D (c) downstream for TSR equals 3.87

Figures 21 and 22 present the distribution of the $\overline{u'v'}/U_\infty^2$ Reynolds stress component for both TSR values in the z-direction. From the offset, it is clear that the tower and nacelle structure are the root source for the majority of the Reynolds stress within the flow. Reynolds stress values are seen to increase considerably when passing through Z/R=0 with interaction between the blade wake and shedding from the nacelle exciting the flow. For TSR equals 3.87 (figure 22), the experimental values of Reynolds stress begin to fluctuate around $Z/R \simeq \pm 0.7$. This coincided with the predicted location of the secondary vortical structure. Overall, the majority of the Reynolds stresses are localized behind the nacelle structure, suggesting that interaction between the wake and the nacelle structure contributes greatly to the stress levels within the flow. Stresses peak at $Z/R = \pm 0.1$ which is close to the root of the blade located at $r/R = 0.12$. It can be seen that the root vorticies for TSR equals 3.87 (figure 22) are stronger than those at TSR equals 2.54 (figure 21). Initial Reynolds stress values associated with the root vorticies at 0.66D are 1.3×10^{-3} and 2.8×10^{-3} for TSR equals 2.54 and 3.87 respectively. However, despite having initially higher levels of shear stress, levels of stress reduce faster for TSR equals 3.87 in comparison to TSR 2.54. Again highlighting a faster degradation of the wake and return to freestream values. The transition from positive to negative values of stress at $Z/R = 0$ is due to the rotation of the root vortex system in the wake. Similar to both figures 21 and 22, the Reynolds stresses within the flow retreat towards 0 in the freestream. Reynolds stress values at TSR equals 3.87 are larger than those for the TSR equals 2.54 case at the Z/R = 0 region. This could be attributed to the stronger root vortices present in this region due to the increased TSR.

Numerical predictions of the Reynolds stresses within the wake in the z-direction for TSR equals 2.54 and 3.87 are presented in figures 21 and 22. The location of maximum percentage error between the computational and experimental results tends to be located at $-0.4 < Z/R < 0.4$ where the flow tends to be the most chaotic behind the nacelle structure and in the root vortex system. The errors in this region are expected due to the over and under-prediction of the rms u' and v' components in this region mentioned earlier. All models do predict a reduction of the Reynolds stresses towards zero at Z/R=$\pm$1, similar to experimental results. The values of Reynolds stress peak at Z/R=$\pm$0.1, which coincides with experimental results. This is evident from 0.66D to 1.5D. There is an overall trend of reduced Reynolds stress values with distance downstream, which indicates the decay of the vortical structures within the wake.

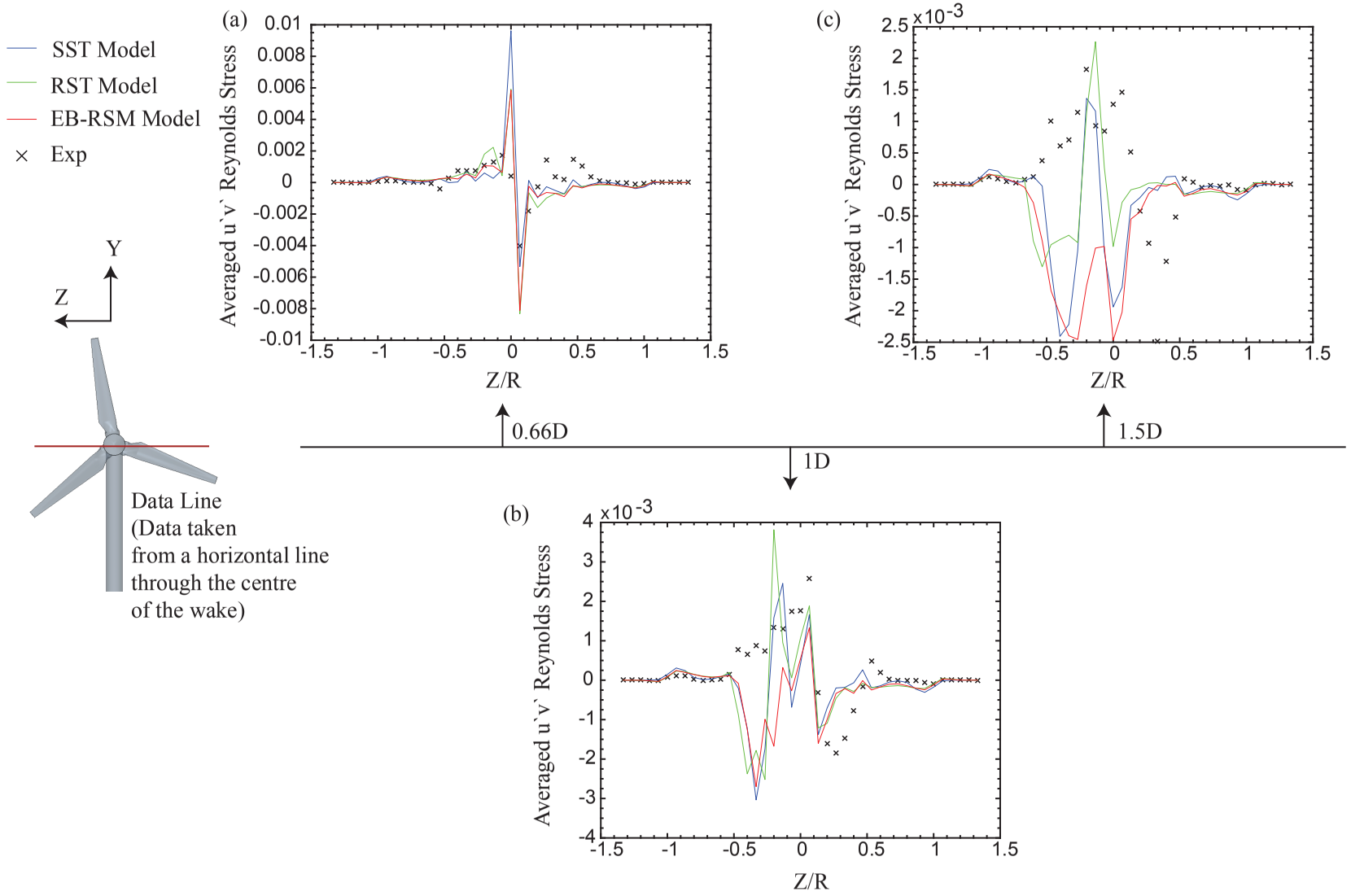

Figure 21: Averaged $u'v'$ Reynolds Stresses at 0.66D (a), 1D (b) and 1.5D (c) downstream for TSR equals 2.54

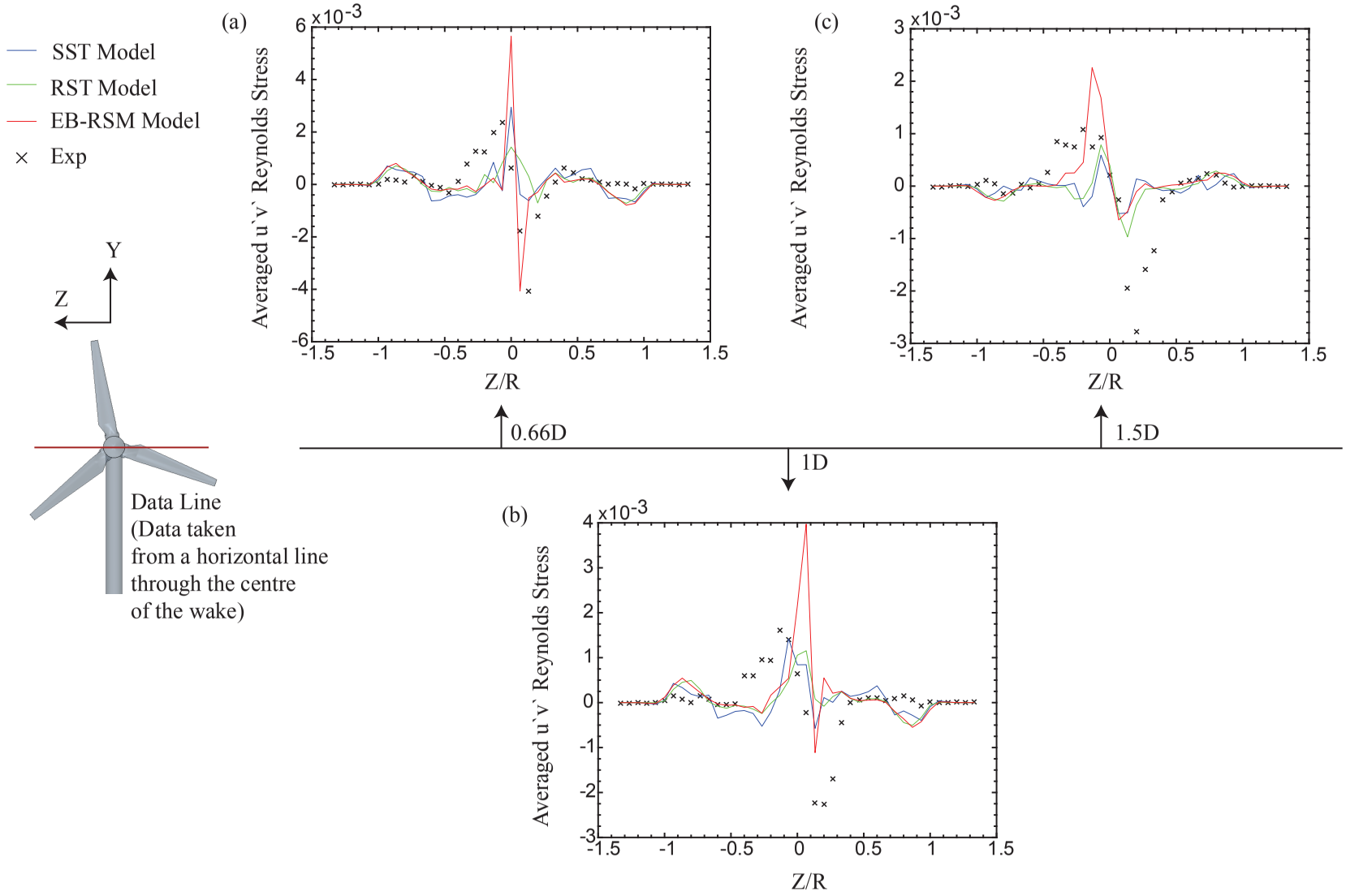

Figure 22: Averaged $u'v'$ Reynolds Stresses at 0.66D (a), 1D (b) and 1.5D (c) downstream for TSR equals 3.87

4.4. Assessment of Turbulence Modelling Strategies Used

As outlined in section 4.3, all models under-predicted the magnitude of the rms u' and v' velocity components in the flow, which was highlighted again when comparing between experimentally recorded and numerically predicted $\overline{u'v'}/U_\infty^2$ Reynolds stress values. However, by comparison of figures 17, 18, 19 and 20, all models tended to predict the inverse Laplace distribution of both the rms u' and v' components (with the exception of the RST model, which struggled to predict accurately the rms u' and v' components with accuracy for TSR value of 3.87), which highlights that all models were able to model the physics of a HAWT wake to varying degrees of accuracy.

Additionally, each turbulence modelling strategy employed, accurately predicted wake velocity deficits with the largest discrepancy between the results of each turbulence modelling strategy occurring when evaluating their ability to predict turbulence in the HAWT wake. Their ability to model velocity fluctuations in the flow is where each model differs the most. This is further supported when considering the RST and EB-RSM models. Both models employed identical physics continua, mesh densities and y^+ wall treatments. The only difference between both models was the pressure strain relationship used by each. The RST model used the linear pressure-strain two-layer relationship of Gibson et al. [39] and the EB-RSM model used the elliptical-blending relationship of Manceau et al. [44]. As outlined in section 4.3, the velocity fluctuations and essentially the origins of turbulence is often developed from the interaction between the fluid flow and the wall.

Discrepancies between the models may highlight where the source of inaccuracy of each model lies. For example, as outlined, each model had the same mesh distribution and y^+ wall treatments. The only difference between the models was the solvers themselves. However, despite this, as shown in section 3.7, each model predicted different maximum and average y^+ values over the turbine blades. Considering that with a higher y^+ value there is less resolution to capture the presence of the turbulent boundary layer. This would undoubtedly result in each blade predicting different velocity profiles at the boundary layer. Additionally, having a combination of y^+ values with values greater and less than unity over the blade could have made resolving the boundary layer difficult for each model. When y^+ values are below unity, the boundary layer is resolved. However, the boundary layer is modelled using wall treatments when the y^+ values are above unity. The over and back between both these methods could have increased the difficulty of solving the boundary layer for each turbulence model. It is unknown if altering the blade mesh such that the y^+ values remain above or below unity during the simulation would have improved the results.

The difference in modelled boundary layers can be highlighted when looking at the wall shear stress values over the rotor. Figure 23 shows the distribution of wall shear stress over the rotor, as predicted by the RST and SST $k-\omega$ models. The EB model predicted similar wall shear stress values in comparison to the SST $k-\omega$ model and therefore, the distribution of wall shear values predicted by the EB model are not shown. It can be seen in figure 23(a) that the SST $k-\omega$ model predicted greater variation in wall shear stress

towards the trailing edge of the blades (highlighted in red). This swirl pattern at the trailing edge is associated with increased shear values and shedding along the length of the blade trailing edge. This is not captured in the RST model and might also explain why the model greatly under-predicted the rms velocity components for a TSR value of 3.

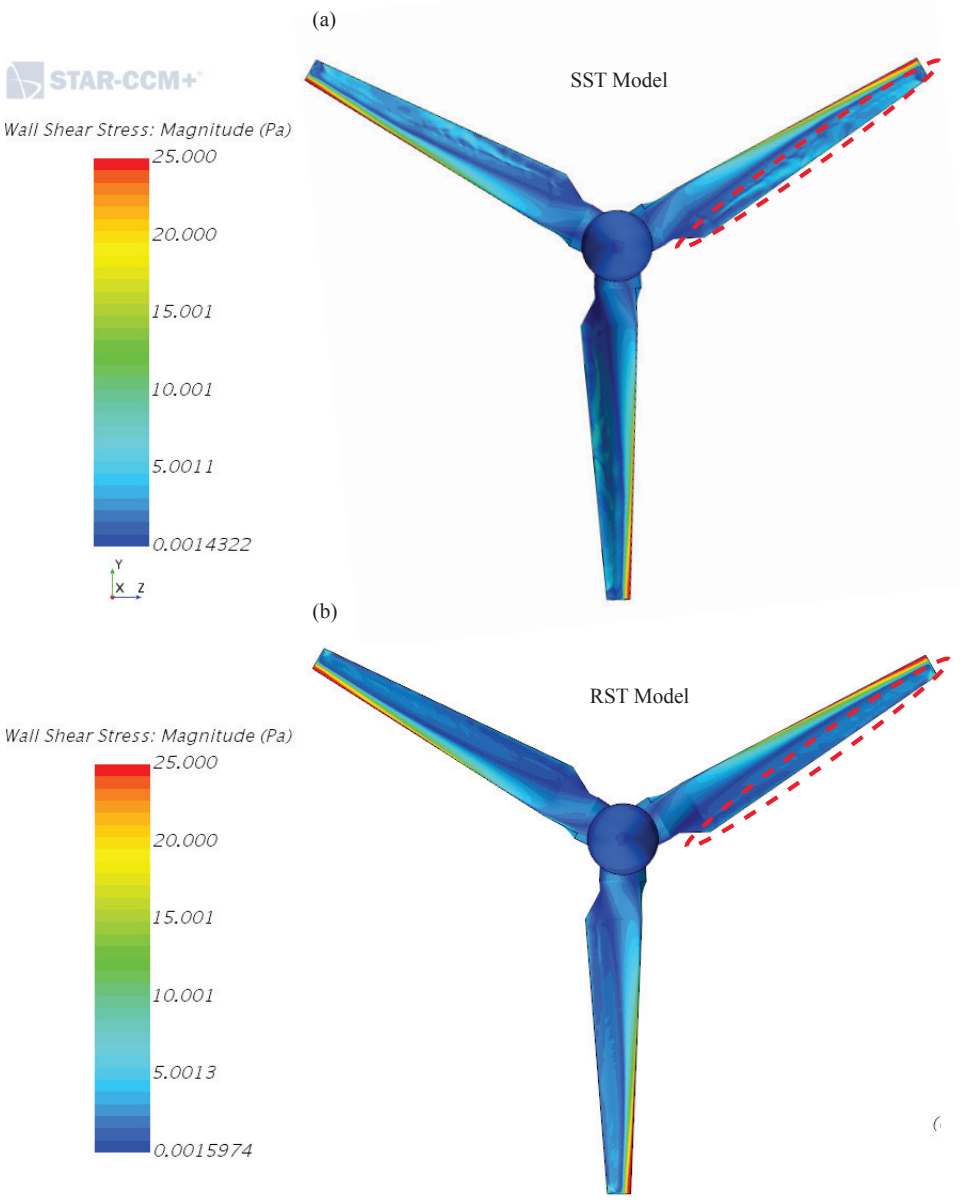

Figure 23: Wall shear stress values over the rotor predicted by SST $k-\omega$ model (a) and RST model (b). TSR = 3.87

A final consideration is the difference in results between the RST and EB-RSM models. The EB-RSM model was developed to be a less intensive version of the RST model as outlined

in section 3.5 by adapting the elliptical blending pressure-strain relationship of Manceau et al. [44]. In the linear pressure-strain approach, the computation is divided into two layers. In the layer adjacent to the wall, the turbulent dissipation rate ϵ and the turbulent viscosity μ_t are specified as functions of wall distance. The formulation is the same as that used in the $k-\epsilon$ model. The two-layer model prescribes values for ϵ algebraically based on distance from the wall in the viscosity dominated near-wall flow regions. This might have resulted in the solver being more sensitive to varying y^+ values in the current study. On the other hand, the EB-RSM model used the standard elliptical blending method of Billard et al. [54], which has been noted to be an improvement on the existing realizable $k-\epsilon$ model in terms of accuracy, especially in the near-wall region. Additionally, as noted by Manceau et al. [44], the elliptic blending strategy allowed for the integration of wall treatments down to the wall without the use of damping functions with one elliptical equation instead of six.

However, the EB-RSM model itself was inaccurate. This could be attributed to the simplification of the model. In order to simplify the model to reduce computational and time costs the model suffered a reduction in accuracy in the prediction of anisotropies in the near wall. Therefore, the model may be unable to accurately model the effects of turbulence in the near wall region. The presence of a solid wall influences turbulent flow through two mechanisms. The first is through viscous effects which require that velocity components in all directions must equal zero at the wall. The second is the blocking effect whereby, due to the impermeable nature of a solid wall, primarily fluctuations in the wall-normal direction are suppressed. This creates highly anisotropic turbulent structures, as noted by Emory et al. [55]. As noted by Manceau et al. [44], the formulation in the EB-RSM resulted in anisotropic structures being poorly captured.

Generally, the numerical simulation results at a TSR value of 2.54 have better agreement with experiment data than those at TSR=3.87. Reduced accuracy for predictions at TSR = 3.87 were attributed to reduced resolution of the boundary layer due to increased rotational speed of the blades (which impacted y^+ values). This complicated the model and made it more difficult for the turbulence models to resolve the turbulent boundary layer as show in figure 23 (illustrating wall shear stress values).

Finally, a Root-Mean-Square-Error (RMSE) analysis was carried out to investigate the overall prediction capabilities of each individual model. The RMSE analysis is presented in tables 1, 2 and 3 for both TSR cases for both mean velocity deficit and rms fluctuating velocities. Over a range of 0–1, the lower the RSME value, the better the behaviour of the numerical model. The maximum RSME value for the mean velocity deficit was 0.083 (RST model predictions at 1D for a TSR value of 3.87) The maximum RSME value for the fluctuating u velocities was 0.028 (RST model predictions at 0.66D for a TSR value of 3.87). The maximum RSME value for the fluctuating v velocities was 0.026 (SST k-ω model predictions at 1D and 1.5D for a TSR value of 2.54).

Table 1: RMSE analysis for mean velocity deficit

Model	X/D	TSR 2.54	TSR 3.87
SST k-ω	0.66	0.062	0.059
RST	0.66	0.058	0.059
EB-RSM	0.66	0.070	0.056
SST k-ω	1	0.061	0.077
RST	1	0.065	0.083
EB-RSM	1	0.032	0.053
SST k-ω	1.5	0.035	0.081
RST	1.5	0.040	0.070
EB-RSM	1.5	0.044	0.082

Table 2: RMSE analysis for fluctuating u velocities

Model	X/D	TSR 2.54	TSR 3.87
SST k-ω	0.66	0.022	0.025
RST	0.66	0.022	0.028
EB-RSM	0.66	0.019	0.023
SST k-ω	1	0.023	0.022
RST	1	0.023	0.024
EB-RSM	1	0.024	0.017
SST k-ω	1.5	0.024	0.021
RST	1.5	0.023	0.021
EB-RSM	1.5	0.024	0.015

Table 3: RMSE analysis for fluctuating v velocities

Model	X/D	TSR 2.54	TSR 3.87
SST k-ω	0.66	0.021	0.018
RST	0.66	0.018	0.019
EB-RSM	0.66	0.021	0.014
SST k-ω	1	0.026	0.015
RST	1	0.024	0.020
EB-RSM	1	0.024	0.013
SST k-ω	1.5	0.026	0.015
RST	1.5	0.025	0.018
EB-RSM	1.5	0.024	0.012

5. Conclusions

Experimental and numerical investigations were carried out to assess the ability of the SST $k-\omega$, RST and EB-RSM turbulence models to accurately model a HAWT wake. A compari-

son was made between the experimentally recorded and numerically predicted wake velocity deficit and turbulence characteristics of the wake. It has been found that all models are capable of predicting the mean flow characteristics within the wake structure of a HAWT. All models predicted the generation and decay of root and tip vortices, and the formation of a central vortex sheet. The values of axial velocity predicted by all models were comparable with experimental results and coincide with previous studies, whereby increasing TSR values reduced the wake velocity deficit. The greatest velocity deficit is consistently located behind the nacelle and tower structure with the tower introducing considerable quantities of recirculating flow to the wake. The tower and nacelle structures, combined with the central vortex system supply a continuous velocity deficit to the wake with the blades only having a periodic effect on the wake velocity deficit, noticeable only after monitoring the wake over a long period of time. The study highlighted that all models could accurately predict the mean flow characteristics of a HAWT wake and, therefore, could accurately predicted rotor loading, also.

Investigation of the rms u' and v' velocities showed that again all turbulence modelling strategies estimated these velocity components to the correct order of magnitude. All models (with the exception of the RST model at a TSR value of 3.87) predicted the rms velocity values to have an inverse Laplace distribution in the wake, similar to experimental results. However, all models under-estimated the magnitude of these velocity values with predictions as low as -43% of experimental results. Peaks in fluctuating velocities at Z/R = 0.8 lead the authors to conclude that a secondary vortex structure formed. Similar to Yang et al. [11] and Whale et al. [6], the structure merged with the tip vortex further downstream (in this case between 1.5D to 2D downstream).

Investigation of the $\overline{u'v'}$ Reynolds stress component showed increased stress levels behind the nacelle. Again, similar to previous studies, stress levels in the wake reduced for higher TSR values with the exception of stress levels in the root vortex region. Overall, all models performed reasonably well, with the majority of errors located at the centre of the wake.

Inaccuracies in the models were attributed primarily to the fluctuating y^+ values over the blades. This is thought to have increased the difficulty for each solver to accurately predict the boundary layer and as shown for the TSR equals 3.87 case, despite using the same mesh and wall treatments, both the SST $k-\omega$ and RST computed different levels of wall shear stress at the trailing edge of the blades. This was concluded to be the reason why the RST model greatly under-predicted rms u' and v' velocities in the wake for a TSR value of 3.87.

The current study was undertaken to investigate the ability of different turbulence models to accurately predict the turbulence characteristics of a HAWT wake. This is important for future FSI simulations as outlined in section 4.3. This study has shown that greater care regarding y^+ values is required as y^+ values tend to fluctuate due to the movement of the blades. The y^+ values should be maintained in one region (either above or below unity in this case) to ensure only one method is used to resolve the boundary layer. This problem

could become increasingly difficult when considering deformable blades and the introduction of atmospheric boundary layers in FSI simulations.

Acknowledgements

This research was funded by the Irish Research Council, Project ID: GOIPG/2013/1265. The authors wish to acknowledge the contribution of all the technical staff at the University of Limerick who manufactured the HAWT model. The authors would also acknowledge the Irish Centre for High End Computing (ICHEC) for the computational resources made available for this study.

References

[1] S. Gomez-Iradi, R. Steijl, G. N. Barakos, Development and Validation of a CFD Technique for the Aerodynamic Analysis of HAWT, Journal of Solar Energy Engineering 131 (3) (2009) 031009–031009–13.

[2] F. Zahle, N. Sørensen, J. Johansen, Wind turbine rotor-tower interaction using an incompressible overset grid method, Wind Energy 12 (6) (2009) 594–619.

[3] Y. Li, K.-J. Paik, T. Xing, P. M. Carrica, Dynamic overset CFD simulations of wind turbine aerodynamics, Renewable Energy 37 (1) (2012) 285–298.

[4] M. Hsu, I. Akkerman, Y. Bazilevs, Finite element simulation of wind turbine aerodynamics: validation study using nrel phase vi experiment, Wind Energy 17 (3) (2014) 461–481.

[5] O'Brien, J.M., and Young, T.M., and O'Mahoney, D.C., and Griffin, P.C., Horizontal axis wind turbine research: A review of commercial CFD, FE codes and experimental practices, Progress in Aerospace Sciences 90 (2017) 1–24.

[6] J. Whale, C. Anderson, R. Bareiss, S. Wagner, An experimental and numerical study of the vortex structure in the wake of a wind turbine, Journal of Wind Engineering 84 (1) (2000) 1–21.

[7] R. Lanzafame, S. Mauro, M. Messina, Wind turbine CFD modeling using a correlation-based transition model, Renewable Energy 52 (2013) 31–39.

[8] A. AbdelSalam, V. Ramalingam, Wake prediction of horizontal-axis wind turbine using full-rotor modeling, Journal of Wind Engineering & Industrial Aerodynamics 124 (2014) 7–19.

[9] G. Yu, X. Shen, X. Zhu, Z. Du, An insight into the separate flow and stall delay for HAWT, Renewable Energy 36 (1) (2011) 69–76.

[10] L. P. Chamorro, F. Porté-Agel, A wind-tunnel investigation of wind-turbine wakes: Boundary-layer turbulence effects, Boundary-Layer Meteorology 132 (2009) 129–149.

[11] Z. Yang, P. Sarkar, H. Hu, An experimental investigation on the wake characteristics of a wind turbine in an atmospheric boundary layer wind, 29th AIAA Applied Aerodynamics Conference 3815 (June) (2011) 1–18.

[12] N. Mandas, F. Cambuli, C. E. Carcangiu, Numerical prediction of horizontal axis wind turbine flow, in: European wind energy conference and exhibition, Athens, Greece, 2006.

[13] D. Hu, O. Hua, Z. Du, A study on stall-delay for horizontal axis wind turbine, Renewable Energy 31 (2006) 821–836.

[14] a. B. R. Fletcher, T.M., D. Kim, O. J. Kwon, Predicting wind turbine blade loads using vorticity transport and rans methodologies, in: Wind Energy Conference and Exhibition, Marseille, France, 2009.

[15] K. Mansour, M. Yahyazade, Effects of turbulence model in computational fluid dynamics of horizontal axis wind turbine aerodynamic, WSEAS transactions on applied and theoretical mechanics 6 (3) (2011) 108–118.

[16] J. Manwell, J. McGowen, A. Rogers, Wind Energy Explained: Theory, Design and Application, 2nd Edition, John Wiley & Sons, Ltd, 2009.

[17] B. Sanderse, Aerodynamics of wind turbine wakes: Literature review, Tech. rep., Energy Research Centre of the Netherlands (2009).
[18] L. Vermeer, J. Sørensen, A. Crespo, Wind turbine wake aerodynamics, Progress in Aerospace Sciences 39 (6-7) (2003) 467–510.
[19] M. Hand, D. Simms, L. Fingersh, D. Jager, J. Cotrell, S. Schreck, S. Larwood, Unsteady aerodynamics experiment phase vi: Wind tunnel test configurations and available data campaigns, Tech. Rep. TP–500–29955, National Renewable Energy Laboratory USA (2001).
[20] W. Zhang, C. Markfort, F. Porté-Agel, Near-wake flow structure downwind of a wind turbine in a turbulent boundary layer, Experimental Fluids 52 (2012) 1219–1235.
[21] P. Durbin, A reynolds stress model for near-wall turbulence, Journal of Fluid Mechanics 249 (1469-7645) (1993) p465–498.
[22] T. Maeda, T. Yokota, S. Y., K. Adachi, Wind tunnel study of the interaction between two horizontal axis wind turbines, Wind Engineering 28 (2) (2004) 197–212.
[23] R. J. Barthelmie, S. Frandsen, M. Nielsen, S. Pryor, P.-E. Rethore, H. Jørgensen, Modelling and measurements of power losses and turbulence intensity in wind turbine wakes at middelgrunden offshore wind farm, Wind Energy 10 (6) (2007) 517–528.
[24] O. DeVries, On the theory of the horizontal-axis wind turbine., Fluid Mechanics 15 (1983) 77–96.
[25] D. Hu, Z. Du, Near wake of a model horizontal-axis wind turbine, Journal of Hydrodynamics, Ser. B 21 (2) (2009) 285–291.
[26] P. Krogstad, M. S. Adaramola, Performance and near wake measurements of a model horizontal axis wind turbine, Wind Energy 15 (5) (2012) 743–756.
[27] Y. Odemark, Wakes behind wind turbines - studies on tip vortex evolution and stability, Ph.D. thesis, Royal Institute of Technology, KTH Mechanics, Stockholm, Sweden (2012).
[28] M. Sherry, J. Sheridan, D. Jacono, Characterisation of a horizontal axis wind turbine's tip and root vortices, Experiments in fluids 54 (1417) (2013) 1–19.
[29] R. Howell, N. Qin, J. Edwards, N. Durrani, Wind tunnel and numerical study of a small vertical axis wind turbine., Renewable Energy 35 (2) (2010) 412–422.
[30] S. McTavish, D. Feszty, F. Nitzsche, An experimental and computational assessment of effects on wind turbine wake development, Wind Energy 17 (10) (2014) 1515–1529.
[31] D. Medici, P. H. Alfredsson, Measurements on a wind turbine wake: 3D effects and bluff body vortex shedding, Wind Energy 9 (3) (2006) 219–236.
[32] K. Vafiadis, N. Stergiannes, A. Tourlidakis, K. Rados, Computational investigation of horizontal axis wind turbine wake, in: EWEA Proceedings 2013, Vienna, Austria, 2013.
[33] D. Wilcox, Turbulence Modeling for CFD, 3rd Edition, DCW Industries, Inc, 2006.
[34] J. Dacles-Mariani, G. Zilliac, J. Chow, P. Bradshaw, Numerical/experimental study of a wingtip vortex in the near field, AIAA Journal 33 (9) (1995) 1561–1568.
[35] T. Craft, A. Gerasimov, B. Launder, C. Robinson, A computational study of the near-field generation and decay of wingtip vortices, International Journal of Heat and Fluid Flow 72 (2006) 684–695.
[36] B. Sanderse, S. Pijl, B. Koren, Review of computational fluid dynamics for wind turbine wake aerodynamics, Wind Energy 14 (7) (2011) 799–819.
[37] J. Steinhoff, N. Lynn, L. Wang, Computation of high reynolds number flows using vorticity confinement: I. formulation, UTSI Preprint.
[38] R. Löhner, On limiters for minimal vorticity dissipation, in: Proceedings of the 47th AIAA Aerospace Sciences Meeting, Orlando, Flordia, USA, 2009.
[39] M. Gibson, B. Launder, Ground effects on pressure fluctuations in the atmospheric boundary layer, Journal of Fluid Mechanics 86 (3) (1978) 491–511.
[40] H. Versteeg, W. Malalasekera, An Introduction to Computational Fluid Dynamics The Finite Volume Method, 2nd Edition, Pearson Education, 2007.
[41] B. Launder, N. Shima, Second-moment closure for the near-wall sublayer: Development and application, American Institute of Aeronautics and Astronautics 27 (10) (1989) 1319–1325.
[42] B. Launder, D. Tselepidakis, B. Younis, A second moment closure study of rotating channel flow,

Physics of Fluids 29 (1986) 38–48.
[43] S. Pope, Turbulent Flows, 11th Edition, Cambridge University Press, 2011.
[44] R. Manceau, K. Hanjalić, Elliptic blending model: A new near-wall reynolds-stress turbulence closure, Physics of Fluids 14 (2) (2002) 744–754.
[45] S. Lardeau, R. Manceau, Computations of complex flow configurations using a modified elliptic-blending reynolds-stress model, in: International Symposium on Engineering turbulence modelling, Marbella, Spain, 2014.
[46] L. Wang, R. Quant, A. Kolios, Fluid structure interaction modelling of horizontal-axis wind turbine blades based on cfd and fea, Journal of Wind Engineering and Industrial Aerodynamics 158 (2016) 11–25.
[47] M. O'Regan, A numerical and experimental investigation of the mean and turbulent characteristics of a wing-tip vortex in the near field, Ph.D. thesis, University of Limerick, Castletroy, Limerick, Ireland (September 2014).
[48] H. Schümann, F. Pierella, L. Sætran, Experimental Investigation of Wind Turbine Wakes in the Wind Tunnel, Energy Procedia 35 (1876) (2013) 285–296.
[49] F. Bertagnolio, N. Sørensen, J. Johansen, P. Fuglsang, Wind turbine airfoil catalogue, Tech. Rep. Report Risø-R-1280(EN), Risø National Laboratory (2001).
[50] E. Anderson, T. Lawton, Correlation between vortex strength and axial velocity in a trailing vortex, Journal of Aircraft 40 (1) (2003) 699–704.
[51] O'Regan, M.S., and Griffin, P.C., and Young, T.M., Numerical and experimental investigation of the mean and turbulent characteristics of a wing-tip vortex in the near field, Proceedings of the institution of mechanical engineers. Part G: Journal of Aerospace Engineering 228 (13) (2014) 2516–2529.
[52] F. Menter, Two-equation eddy-viscosity turbulence modelling for engineering applications, AIAA Journal 32 (8) (1994) 1598–1605.
[53] R. Gómez-Elvira, A. Crespo, E. Migoya, F. Manuel, J. Hernández, Anisotropy of turbulence in wind turbine wakes, Journal of wind engineering and industrial aerodynamics 93 (10) (2005) 797–814.
[54] F. Billard, D. Laurence, A robust $k - \epsilon - v^2$ elliptic blending turbulence model applied to near-wall, separated and buoyant flows, International Journal of Heat and Fluid Flow 33 (1) (2012) 45–58.
[55] M. Emory, G. Iaccarino, Annual research briefs - 2014 center for turbulence research - stanford university (2014).